The very-high resolution configuration of the EC-Earth global model for HighResMIP

Eduardo Moreno-Chamarro, Thomas Arsouze, Mario Acosta, Pierre-Antoine Bretonnière, Miguel Castrillo, Eric Ferrer, Amanda Frigola, Daria Kuznetsova, Eneko Martin-Martinez, Pablo Ortega, et al.

1
2

The very-high resolution configuration of the
EC-Earth global model for HighResMIP

3
4

5 Eduardo Moreno-Chamarro[1,2*], Thomas Arsouze[1,3], Mario Acosta[1], Pierre-Antoine Bretonnière[1],

6 Miguel Castrillo[1], Eric Ferrer[1], Amanda Frigola[1], Daria Kuznetsova[1], Eneko Martin-Martinez[1],

7 Pablo Ortega[1], Sergi Palomas[1]

8
9

10 1. Barcelona Supercomputing Center (BSC), Barcelona, Spain

11 2. Now at: Max Planck Institute for Meteorology, Hamburg, Germany

12 3. Now at: CIRAD, UMR AMAP, F-34398 Montpellier, France

13 * Corresponding author: eduardo.chamarro@mpimet.mpg.de

14
15
16
17
18
19
20
21
22
23
24
25
26
27
28
29
30

Abstract

We here present the very-high resolution version of the EC-Earth global climate model, EC-Earth3P-VHR, developed for HighResMIP. The model features an atmospheric resolution of ~16 km and an oceanic resolution of 1/12° (~8 km), which makes it one of the finest combined resolutions ever used to complete historical and scenario-like CMIP6 simulations. To evaluate the influence of numerical resolution on the simulated climate, EC-Earth3P-VHR is compared with two configurations of the same model at lower resolution: the ~100-km-grid EC-Earth3P-LR, and the ~25-km-grid EC-Earth3P-HR. The models' biases are evaluated against observations over the period 1980–2014. Compared to LR and HR, VHR shows a reduced equatorial Pacific cold tongue bias, an improved Gulf Stream representation with a reduced coastal warm bias and a reduced subpolar North Atlantic cold bias, and more realistic orographic precipitation over mountain ranges. By contrast, VHR shows a larger warm bias and overly low sea ice extent over the Southern Ocean. Such biases in surface temperature have an impact on the atmospheric circulation aloft, with improved stormtrack over the North Atlantic, yet worsened stormtrack over the Southern Ocean compared to the lower resolution model versions. Other biases persist with increased resolution from LR to VHR, such as the warm bias over the tropical upwelling region and the associated cloud cover underestimation, and the precipitation excess over the tropical South Atlantic and North Pacific. VHR shows improved air–sea coupling over the tropical region, although it tends to overestimate the oceanic influence on the atmospheric variability at mid-latitudes compared to observations and LR and HR. Together, these results highlight the potential for improved simulated climate in key regions, such as the Gulf Stream and the Equator, when the atmospheric and oceanic resolutions are finer than 25 km in both the ocean and atmosphere. Thanks to its unprecedented resolution, EC-Earth3P-VHR offers a new opportunity to study climate variability and change of such areas on regional/local spatial scales, in line with regional climate models.

1. Introduction

Interest in high-resolution modeling has soared in the past years, specially thanks to large European research projects and initiatives such as PRIMAVERA, nextGEMS, EERIE, and Destination Earth (last access: 20 June 2024). Broadly, these projects seek to build the next generation of high-resolution global climate (or Earth system) models capable of representing

62 climate phenomena with unprecedented accuracy, to simulate and predict regional climate, guide

63 policymaking, and provide relevant climate information to end users. Thanks to these efforts,

64 high-resolution models at resolutions of 25–50 km or even finer have been proved to lead to

65 reduced biases in the simulated climate (see Introduction in Moreno-Chamarro et al., 2022 for a

66 review), and to a better representation of, for example, tropical cyclones (Roberts et al., 2020a;

67 Vidale et al., 2021; Zhang et al., 2021), storm-tracks (e.g., Hodges et al., 2011), the intertropical

68 convergence zone (ITCZ; e.g., Doi et al., 2012; Tian et al., 2020), or the Gulf Stream and

69 associated air–sea interactions (e.g., Kirtman et al., 2012; Bellucci et al., 2021) compared to

70 standard resolution models (hereafter, ~100-km grid). An extensive review of the benefit of

71 high-resolution modeling can be found in Haarsma et al. (2016), Hewitt et al. (2017), Roberts

72 M.J. et al. (2018), and Czaja et al. (2019). However, increased model resolution alone is not

73 always the answer: for example, persistent, well-known biases in clouds and radiation can be

74 insensitive to an increase in atmospheric resolution from a ~100-km grid to a 25–50-km grid

75 (Moreno-Chamarro et al., 2022). Inadequate model physics or insufficient tuning can thus mask

76 or negate the benefits of increased resolution.

77   High-resolution modeling faces additional challenges. One is the large computational cost

78 needed to complete the simulations, which also limits the model throughput. Both issues have

79 gradually improved thanks to steady increases in supercomputing power and parallel

80 enhancements in model efficiency to leverage that power. The community trusts in High

81 Performance Computing (HPC) to increase the performance of climate models, developing

82 different approaches to speed models up. These approaches can go from improving the

83 traditional parallelization algorithms (Tintó Prims et al., 2019a) or reducing the accuracy of the

84 variables from double to single precision (Tintó Prims et al., 2019b) to increasing the

85 Input/Output throughput of complex model configurations (Xepes-Arbós et al., 2022). Faster

86 models are also needed to complete, in a reasonable time, the tuning and the spin-up phases,

87 which for a high-resolution model, can be extremely costly. The demand for high efficiency in

88 high-resolution modeling has therefore accelerated the development and implementation of new

89 modeling strategies to ensure an optimal use of the computing resources.

90   High-resolution models also need to find a fair compromise between the resolutions of the

91 different climate components, which, sometimes, can be very disparate—for example, an

92 eddy-rich ocean model (~10 km grid) coupled to a 25 km, 50 km, or even coarser-grid

93 atmosphere model (e.g., Gutjahr et al., 2019). Tsartsali et al. (2022), for example, reported

94 increased ocean–atmosphere coupling strength and better agreement with reanalysis and

95 observations over the Gulf Stream, when both the ocean and atmosphere resolutions are

96 increased to comparable ~25-km grid at least. Moreton et al. (2021) showed a degraded

97 representation of the air–sea interaction at increased oceanic resolution but a constant

98 atmospheric resolution. Similarly, Ma et al. (2016) found that the mesoscale ocean temperature

99 affects the storm track over the Pacific only when the atmospheric model resolution is enough to

100 resolve the small-scale diabatic heating. Finally, Rai et al. (2023) described a disproportionate

101 eddy killing when a coarse 200-km wind forcing is used to force a finer (~10–25-km) ocean,

102 compared to the case with similar grid sizes. These results of these studies thus advocate for a

103 similar resolution in both the atmosphere and ocean.

104　　High-resolution modeling usually relies on single-model component, either atmospheric-only

105 (Baker et al., 2019) or ocean-only configurations (e.g., Biastoch et al., 2021), or on regional

106 models (e.g., Woollings et al., 2010; Ma et al., 2017) as in CORDEX (Jacob et al., 2014) for

107 hypothesis testing and downscaling climate projections. Such configurations, however, lack

108 global energy constraints, remote influences, and, potentially, key feedbacks rectifying the mean

109 state. These models are also limited by the boundary conditions, which often are derived from

110 coarser (~100 km) global models and can present biases in their mean climate that might be

111 absent or much reduced at a higher resolution; these biases might then be passed onto the single

112 model configurations. For example, an overly smooth Gulf Stream temperature gradient, an

113 incorrect separation, or the lack of mesoscale in ocean temperatures can impact the response of

114 the atmospheric circulation aloft (e.g., Ma et al., 2017; Lee et al., 2018). Low-resolution and

115 high-resolution global models can also respond differently to climate change: for example, the

116 northward shift and strong surface warming of the Gulf Stream projected by the eddy-rich

117 configuration of the HadGEM3-GC3.1 model for the 21st century is absent at the

118 lower-resolution model versions (Moreno-Chamarro et al., 2021). Associated with this, the

119 increase in winter precipitation is similarly much larger over Europe at the highest resolution

120 than at any lower one, which reinforces the idea that the response of the atmosphere is strongly

121 sensitive to the boundary conditions. These findings put a limit to our confidence in single-model

122 configurations and regional models, since they lack a global dynamical response.

123 As a response to the listed challenges, we here present the eddy-rich version of the EC-Earth
124 climate model for PRIMAVERA/HighResMIP. This is likely one of the finest combined
125 horizontal resolution global models ever used to complete CMIP-like simulations, with a
126 nominal resolution of about 10–15 km; it also has the additional advantage that the resolution is
127 comparable in both the atmosphere and ocean/sea-ice, which allows the atmosphere to "see" the
128 fine-scale forcing from the ocean with minimal information lost from interpolation. In this paper,
129 we describe the model configuration and the developments in model efficiency (Section 2), as
130 well as the main characteristics of its climate for the period 1980–2014 compared to observations
131 (Section 3).

132

133 2. Model Description and Experimental Setup

134 2.1 Model description

135 All HighResMIP contributions with the EC-Earth global coupled climate model have been
136 performed with its version 3.2.2, developed within the PRIMAVERA project (EC-Earth3P). The
137 model consists of the atmosphere, ocean, and sea ice components. The atmosphere model is
138 based on the ECMWF Integrated Forecasting System (IFS), in the 36r4 cycle. A detailed account
139 of the changes introduced in this cycle can be found on the ECMWF website
140 (https://confluence.ecmwf.int/display/FCST/Implementation+of+IFS+Cycle+36r4, last access:
141 20 June 2024). The very-high resolution version of the model, EC-Earth3P-VHR, features a
142 triangular truncation at wave number 1279 (hence known as T1279) in spectral space, with a
143 linear N640 reduced Gaussian grid. This corresponds to a spacing of ~16 km. However, because
144 of the complexity of numerical solutions and parametrizations, the effective resolution (this is the
145 smallest scale IFS T1279 can fully resolve) is of ~120 km (Abdalla et al., 2013). Vertically, the
146 model features 91 levels, resolving the middle atmosphere up to 0.01 hPa. The model time step
147 during the simulation was 360 s. IFS integrates the revised land surface hydrology Tiled
148 ECMWF Scheme for Surface Exchanges over Land (H-Tessel) model (Balsamo et al., 2009;
149 Hazeleger et al., 2012).

150 The ocean model is the Nucleus for European Modelling of the Ocean in its version 3.6
151 (NEMO3.6; Madec, 2008, Madec and the NEMO team, 2016). This is a hydrostatic,
152 finite-difference, free-surface, primitive equation general circulation model. EC-Earth3P-VHR
153 uses the ORCA12 tripolar grid, with the horizontal resolution increasing from the Equator to the

154 poles: ~9 km at the Equator, ~7 km at mid-latitudes, and ~2 km near the poles. This corresponds

155 to an effective resolution of ~45 km (roughly five times the ORCA grid spacing). The model

156 uses a z* coordinate system for the vertical grid and has 75 vertical levels, with the resolution

157 decreasing from 1 m at the surface to 200 m in the deep ocean. The bottom topography is derived

158 from the combination of ETOPO1 (Amante and Eakins, 2009) and GEBCO_08 (Becker et al.,

159 2009). The sea ice model is the Louvain-la-Neuve sea Ice Model in its version 3 (LIM3)

160 (Vancoppenolle et al., 2012). This is a dynamic-thermodynamic sea ice model, with five ice

161 thickness categories. The time steps are 240 s for NEMO3.6, and 720 s for LIM3 in the

162 EC-Earth3P-VHR.

163   The atmosphere–land and ocean–sea-ice components are coupled through the OASIS

164 (Ocean, Atmosphere, Sea Ice, Soil) coupler, version 3 (Valcke and Morel, 2006; Craig et al.,

165 2017). The remapping of runoff from the atmospheric grid points to runoff areas on the ocean

166 grid was re-implemented to be independent of the grid resolution. This was done by introducing

167 an auxiliary model component and relying on the interpolation routines provided by the OASIS

168 coupler.

169   EC-Earth3P-VHR (hereafter, VHR) is compared with two lower-resolution global model

170 versions, also run within the PRIMAVERA/HighResMIP project: EC-Earth3P (hereafter, LR;

171 EC-Earth Consortium, 2019), and EC-Earth3P-HR (hereafter, HR; EC-Earth Consortium, 2018).

172 In the atmosphere, they use the T255 (~107 km) and T511 (~54.2 km) spectral resolution of the

173 IFS model respectively (equivalent to an effective resolution of ~600 km and ~280 km

174 respectively; Abdalla et al., 2013), both with 91 vertical levels. In the ocean, LR and HR use the

175 ORCA1 (~100 km) and ORCA025 (~25 km) tripolar grid respectively (equivalent to an effective

176 resolution of ~500 km and ~125 km respectively), both with 75 vertical levels. They both use the

177 LIM3 sea ice model and the OASIS coupler as well. LR and HR's time steps are respectively

178 2700 s and 900 s in all the atmosphere, ocean, and sea ice. More details of these two other model

179 versions can be found in Haarsma et al. (2020).

180   Following the CMIP6 HighResMIP protocol, no additional tuning is applied across

181 resolutions but for a short list of parameters that explicitly change with resolution, particularly

182 for oceanic diffusion and viscosity. The higher resolution in the atmosphere results in a better

183 representation of features such as tropical storms, land/sea transitions, heavy rainfall, and fronts

184 (see Fig. 1 as an example), while in the ocean the increase in resolution allows mesoscale

185 processes to be resolved at a much larger range of latitudes and the representation of finer

186 resolution bathymetric features and coastlines.

187 **2.2 Configuration and workflow setup and performance optimization**

188 The development and maintenance of the EC-Earth model is supported by the EC-Earth

189 Consortium, which shares model code, configurations, and minimal software infrastructure to

190 operate it. While the LR and HR configurations of EC-Earth-3P were developed in a broad

191 collaboration of all the consortium members participating in PRIMAVERA, VHR's development

192 was primarily completed at the Barcelona Supercomputing Center, in collaboration with the

193 Swedish Meteorological and Hydrological Institute (SMHI) within the ESiWACE2 H2020

194 project (last access: 20 June 2024). The development was conducted on two different

195 supercomputing machines: MareNostrum3, and MareNostrum4 (last access: 20 June 2024).

196 VHR's configuration, at the time of the project, represented one of the most cutting-edge

197 versions of a climate model to run over long time scales. Obtaining a production version of the

198 model, however, entailed the development of novel source code and execution scripts, the

199 generation of all requisite files for initializing the simulations, and the adaptation of the model

200 workflow software. This presented a significant challenge for both the operations department and

201 the workflow developers, which were required to fine-tune the system to achieve stable runs and

202 minimize the loss of computing hours. For example, generating the interpolation weight files to

203 couple the new model grids for the OASIS coupler was particularly challenging. This process

204 could not readily be parallelized at that time and required collaborating with the OASIS

205 development group. For the workflow, a significant proportion of the effort was devoted to

206 integrating the dedicated data transfer nodes available in the MareNostrum4 cluster into the

207 workflow. Additionally, the automatic algorithm that enables the suppression of land grid

208 subdomains in the NEMO ocean model was incorporated, resulting in a reduction of about 12%

209 in the required HPC resources. Finally, the MareNostrum4 new network, despite its fast and

210 responsive nature, proved to be quite unstable when subjected to high workloads involving

211 multiple concurrent communications, as was the case of the VHR configuration. At the end of

212 the ESiWACE2 project (December 2022), all the code was versioned and shared with the other

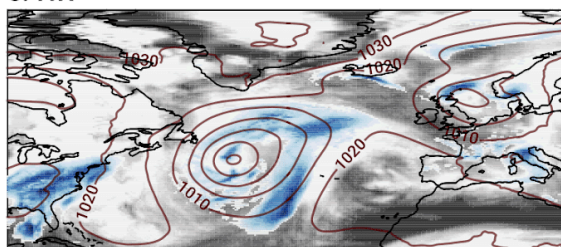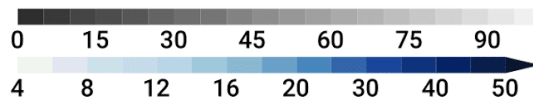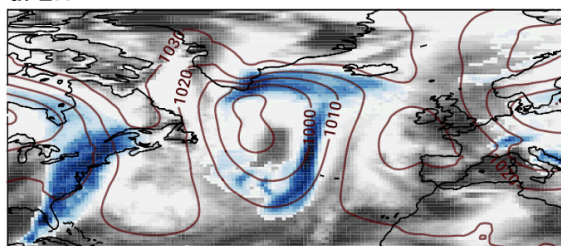213 partners within the EC-Earth Consortium.
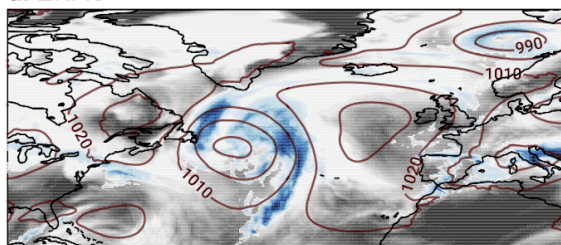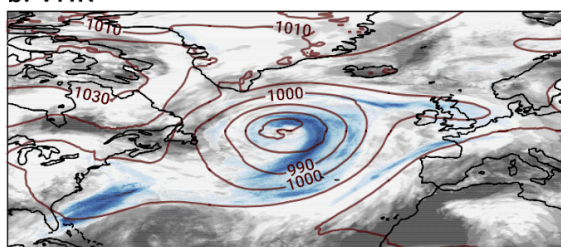
Figure 1. Snapshot of an extratropical storm over the North Atlantic in the winter 1999–2000 in
a) ERA5, and in the b) VHR, c) HR, and d) LR models on their original grids. Shown are daily
precipitation rate (mmd^{-1}; blue shading), cloud cover (% of area; gray shading), and sea-level
pressure (hPa; contours).

220   Once deployed, the workflow needed to be made more efficient to be put into operation.
221 Emerging advancements in global climate modeling demand heightened focus on HPC,
222 particularly to accommodate the increasing need for enhanced model resolution (Acosta et al.,
223 2024). An example of such demanding requirements is the VHR configuration, underscoring the
224 need for efficient resource use. In order to address this issue, we conducted a two-fold HPC
225 performance exercise, which involved both a pure computational performance analysis and a
226 scalability study for each model component (IFS and NEMO), complemented with a load
227 balance optimization for the coupling. This analysis concluded that the coupling and output
228 process could be a bottleneck. An optimization was included to package different coupling fields
229 to be sent in the same MPI (Message Passing Interface) communications, reducing the latency
230 and taking advantage of the bandwidth. Additionally, the I/O (Input/Output) setup was optimized
231 to ensure minimal time was needed to produce the outputs. While the primary objective of the
232 scalability and load-balance study was to assess the model's efficiency and determine an optimal
233 resource utilization, findings by Acosta et al. (2023) also indicate that enhancing the
234 performance of one component, such as reducing the execution time of IFS, may not necessarily
235 decrease the overall execution time of the coupled model. This discrepancy could stem from a
236 synchronization point at the end of each coupled time step, where both components exchange
237 fields. In cases where other non-optimized components lag behind, a load rebalance becomes
238 necessary.

239   We ran a series of scalability tests to balance the resources (computing cores) of the VHR's
240 IFS and NEMO models (Fig. 2). To find the most balanced configuration for a given amount of
241 resources, we followed two different but complementary approaches. The first and most costly
242 one tried to find the optimal distribution by assigning the same number of processors to IFS and
243 NEMO first, and moving resources between them alternately; this allowed identifying the
244 intervals for which the model performance increases by using variations of half-interval search
245 algorithm. The second approach to balance the configuration started from one separate
246 scalability test for each model component that was later used to determine the optimal
247 configuration.

248

249

250
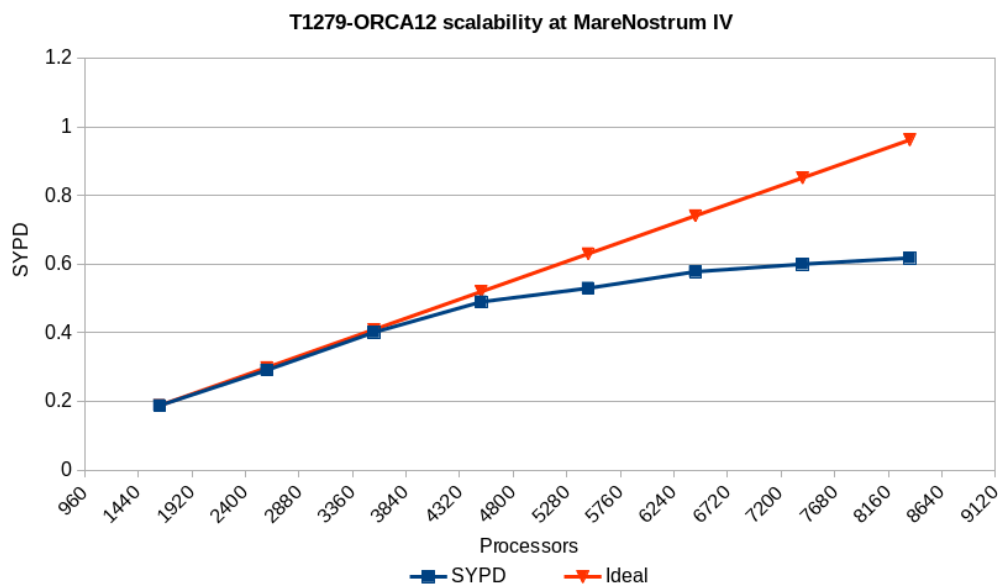
Figure 2. Results of the scalability test of the VHR configuration (T1279 IFS and ORCA12 NEMO) at MareNostrum4 (blue line) in simulated years per day (SYPD) for a given amount of processors. The orange line shows the ideal case with no loss in computing performance.

The simulations described here were configured and run with the workflow manager Autosubmit (Manubens-Gil et al., 2016). This Python toolbox facilitates the production of numerical experiments, like the EC-Earth ones. It creates an oriented graph, taking into account every step of the workflow, including data pre- and post-processing, the transfer to storage spaces, or the conversion of the output data to CMOR standard, with details on computing resources needed for each step. Autosubmit also allows easily handling experiments with different members, start dates, and initial conditions.

2.3 Simulations

The VHR simulations follow the HighResMIP experimental protocol (Haarsma et al., 2016) and consist of: i) a 50-year spin-up run (spin-up-1950), with initial conditions of temperature and salinity from an ocean state representative of the 1950s (Good et al., 2013, EN4 data set) and forcing consisting of well-mixed greenhouse gases, including O_3 and aerosol loading for a 1950s (∼10-year mean) climatology; ii) a 105-year control run (control-1950), starting from the end of

270 spin-up-1950 and keeping the same fixed forcing; iii) the historical run (hist-1950), starting from

271 the same initial state as the control, but with time-varying external forcing for the period

272 1950–2014; iv) and the future scenario run (highres-future), as a continuation of the historical

273 simulation under the CMIP6 SSP5-8.5 scenario (Kriegler et al., 2017) for the period 2015–2050.

274 In this work, VHR's hist-1950 simulation is compared with corresponding hist-1950 runs from

275 LR and HR (Haarsma et al., 2020).

276 During the model setup, we erroneously applied the EN4 initial conditions at the beginning

277 of all the spin-up runs. While EN4 uses practical salinity and potential temperature, the NEMO

278 model, which uses the TEOS-10 equation of state, requires absolute salinity and conservative

279 temperature. Nonetheless, the differences between the two temperature and salinity types is

280 indeed small (Pawlowicz, 2013; McDougall et al., 2021), and we expect the error to minimize

281 throughout the spin-up.

282

283 *2.4 Observations and reanalysis*

284 As we mainly aim to evaluate the performance of EC-Earth3P-VHR configuration and describe

285 the main model biases and characteristics, we focus on the best-observed part of the historical

286 period of the historical simulations, between 1980 and 2014. The three model configurations are

287 compared with the following observational and reanalysis data: near-surface (2 m) air

288 temperature (SAT), zonal winds, sea-level pressure, and turbulent fluxes from the ERA5

289 reanalysis (Hersbach et al., 2020); precipitation rate from the version-2 GPCP dataset (Adler et

290 al., 2003); cloud cover from the version-3 ESA Cloud_cci dataset (ESA CCI-CLOUD; Stengel et

291 al., 2020); potential temperature and salinity of the ocean from the Hadley Center EN4 (version

292 4.2.2; Good et al., 2013); sea ice concentration from OSI SAF (OSI-409/OSI-409-a;

293 EUMETSAT Ocean and Sea Ice Satellite Application Facility, 2015); and sea ice volume from

294 GIOMAS (Global Ice-Ocean Modeling and Assimilation System; Zhang and Rothrock, 2003).

295 The period of comparison maximizes data availability and is therefore 1980–2014 for all the

296 cases but for the GPCP dataset (1983–2014) and the ESA CCI-CLOUD dataset (1982–2014).

297 Biases in sea-surface temperature (SST) are very similar to those in SAT and are therefore not

298 shown.

299

300

11

3. Results

3.1 Spin-up phase

Across all three model resolutions, the length of the spin-up (50 years) appears to be insufficient to equilibrate the full ocean (Fig. 3b); in fact; the ocean temperature is still drifting about 0.001–0.002 °C/yr (computed over the last 50 years) towards warmer conditions at the end of the control simulation in the three configurations. In the upper ocean, however, VHR shows the smallest warming drift of the three configurations: about 0.00005 °C/yr compared to 0.0025 °C/yr and 0.0062 °C/yr in HR and LR, respectively (computed over the last 50 years; Fig. 3a). It is therefore safe to say that an analysis focused on the upper ocean and on the air–sea interface will enjoy a relatively stable climate in the control simulations. In the historical simulations, the warming of the ocean accelerates due to the CO_2 forcing; after 64 years (year 114 in Fig. 3), the whole ocean warming reaches similar values to those at the end of the control simulations after 100 years in the three model resolutions. Near the surface, the warming trend is much larger. Of the three configurations, VHR is the one with the smallest drift in the control run and the smallest ocean warming in the historical period. Although the three runs start from similar initial conditions derived from an EN4 climatology (Section 2.3), VHR is ~0.4 °C warmer near the surface than LR and HR, especially over the spin-up period. This is likely related to the development of a widespread warm bias over the Southern Ocean (Fig. 4), which we discuss in detail in Section 3.6.

In the following Sections, we describe the main characteristics of the VHR compared to LR and HR by focusing on particular regions and biases. This approach should help us highlight the benefits, or lack thereof, due to increased resolution. The main biases in the three model configurations are compared with the observational data set listed in Section 2.4.
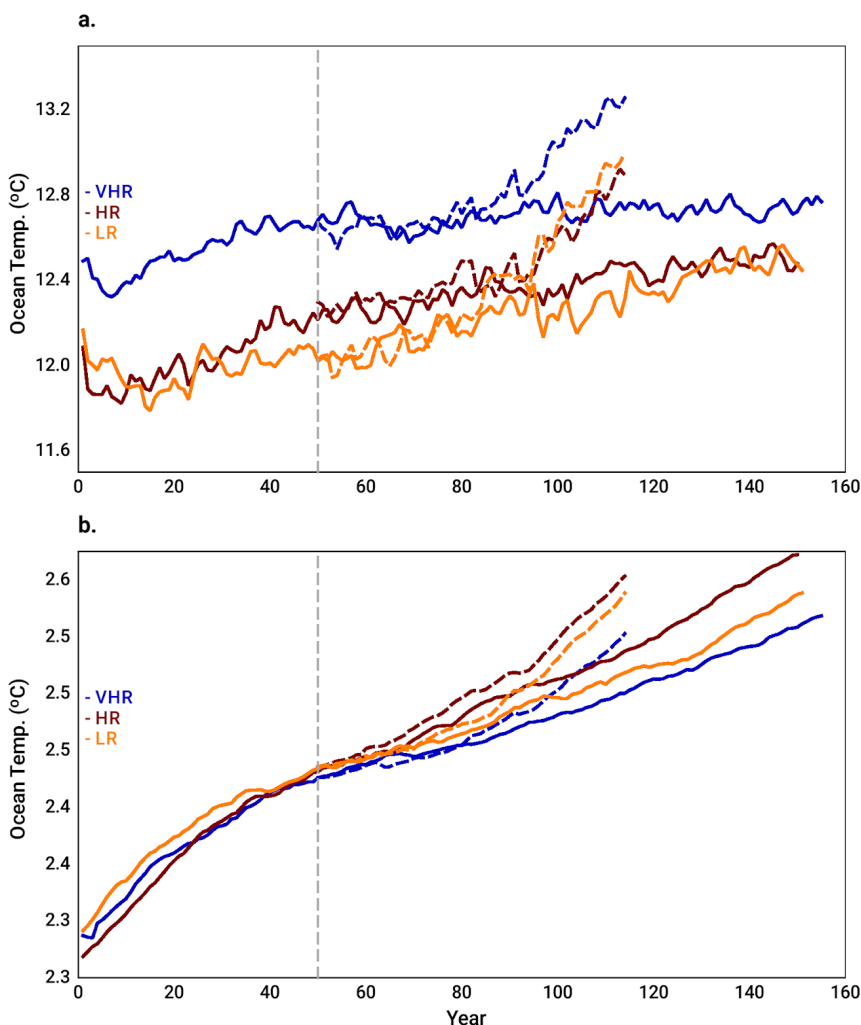
Figure 3. Mean oceanic temperature in the LR (yellow), HR (red), and VHR (blue) models in the spin-up runs (0–50-year period), control runs (50–150-year period; solid lines), and historical runs (50–114-year period; dashed lines) in a) the upper 100 m, and b) the whole ocean. The vertical dashed line marks the end of the spin-up period

3.2 Tropics

A warm bias of 1–2 K is present over the subtropical upwelling regions along the South American and African coasts in the three configurations and shows small variations across them (Fig. 4). The increase in resolution in VHR has thus no clear benefit to reduce it. Past studies

335 have related this bias to an underestimation of the stratocumulus cloud deck (Richter, 2015). This
336 also seems to be the case in the three models, which all show negative cloud biases by about 20
337 % over all the subtropical upwelling areas, specially along the subtropical Pacific and Atlantic
338 western coasts (Fig. 5). A better resolved orography near the region does not contribute to
339 reducing the bias either, as suggested in previous studies (Milinski et al., 2016): for example,
340 although VHR shows reduced temperature biases along the Andes compared to HR and LR, it
341 has no effect on the biases over the eastern subtropical Pacific upwelling.

342　　　Overall, VHR shows reduced tropical precipitation biases compared to HR and LR (Fig. 6).
343 This is the case, for example, for the double ITCZ bias: this bias is usually characterized by a
344 precipitation excess over the central tropical North Pacific and the western tropical South Pacific
345 and a precipitation deficit over the equatorial Pacific, as LR clearly shows. The dry area over the
346 Equator is reduced with resolution, and the anomaly is even non-significant in VHR. This is a
347 clear improvement from increased resolution, and it can be related to a reduced cold bias over
348 the Equator (Fig. 4). In contrast, the precipitation excess over the tropical North Pacific and the
349 Maritime Continent persists into VHR, with only minor reductions of 1–2 mmd^{-1} compared to
350 HR and LR (Fig. 6). The precipitation excess over the tropical North Pacific suggests a seasonal
351 cycle reaching too far north, while the excess over the Maritime Continent, together with that
352 over the western tropical Atlantic and Indian oceans, suggests an excess in convective
353 precipitation over very warm waters.

354　　　Over the tropical Atlantic, the precipitation bias pattern points to an ITCZ anchored to the
355 south-western part and not reaching the Sahel area. This bias is somewhat reduced in VHR
356 compared to HR and LR, although not entirely removed. Over land, the dry bias over North
357 Brazil and the wet bias along the Andes are not reduced with resolution, either. These positive
358 and negative precipitation biases appear together with positive and negative biases in cloud
359 cover, respectively, related to an overestimation or underestimation in convective clouds (Fig. 5).
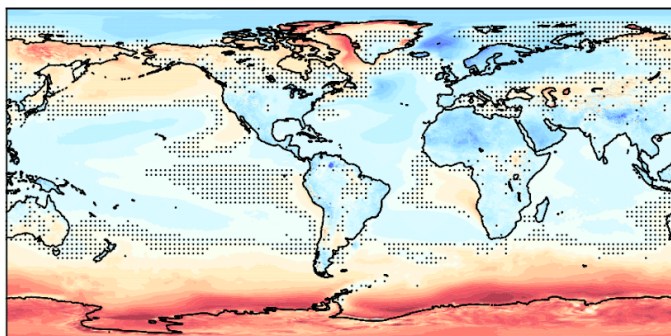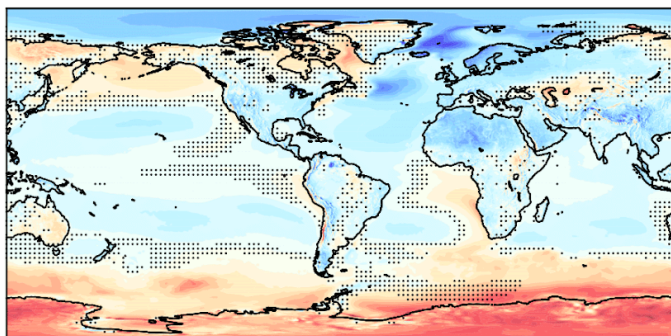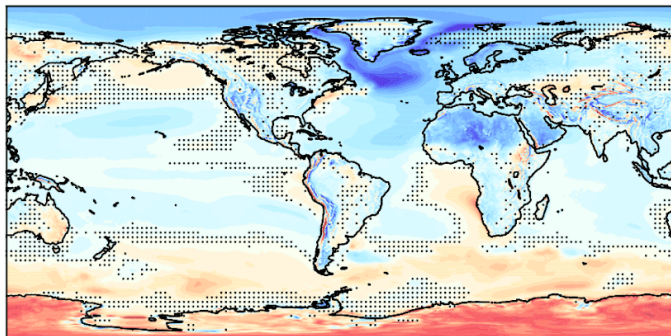
360

361

362

363

364

365

a. VHR

b. HR

c. LR
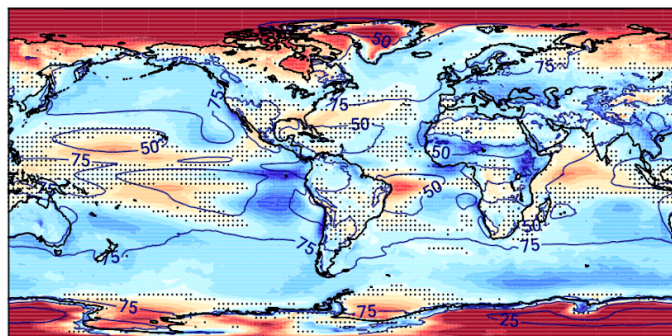
Figure 4. Bias in SAT (in K) with respect to ERA5in the a) VHR, b) HR, and c) LR models for the period 1980–2014. Stippling masks anomalies that are not significant at the 5 % level.
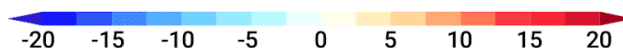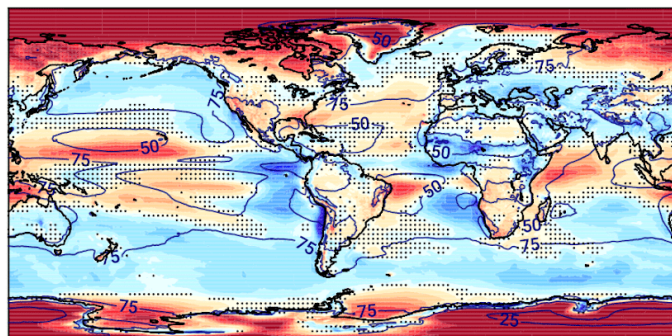
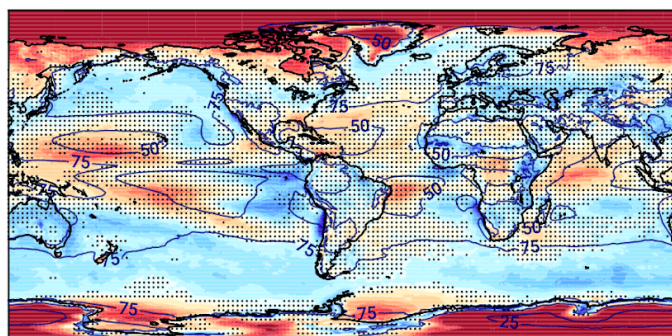**Figure 5.** Bias in cloud cover (in %) with respect to ESA CCI-CLOUD (contours in all the panels; in %) in the a) VHR, b) HR, and c) LR models for the period 1982–2014. Stippling masks anomalies that are not significant at the 5 % level.
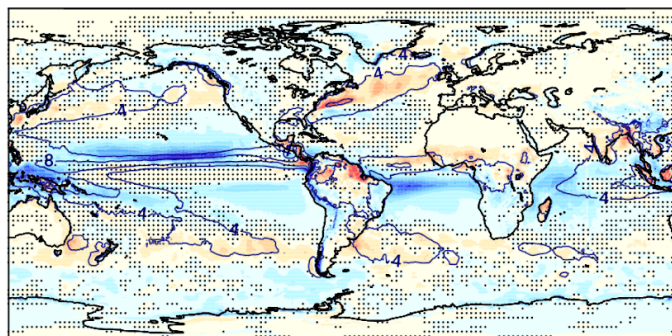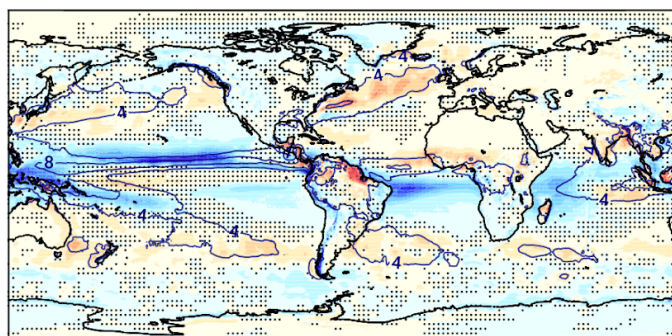
Figure 6. Bias in precipitation rate (in mmd^{-1}) with respect to GPCP (contours in all the panels; in mmd^{-1}) in the a) VHR, b) HR, and c) LR models for the period 1983–2014. Stippling masks anomalies that are not significant at the 5 % level.

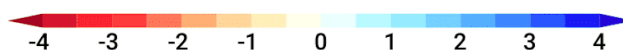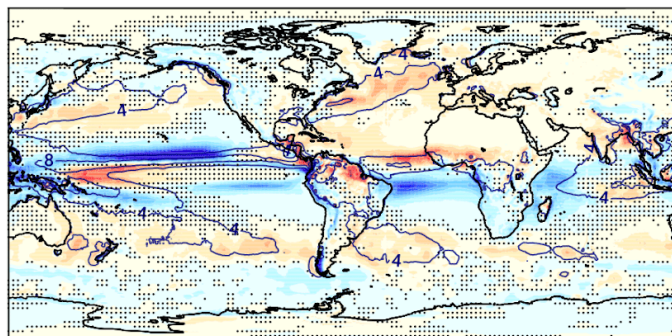### 3.3 Northern Hemisphere mid- and high-latitudes

The largest improvement in the simulated climate from LR to VHR is over the North Atlantic. From south to north, the Gulf Stream representation is much improved in VHR compared to HR and LR, with sharper gradients in temperature and sea-surface height (not shown). The position of the Gulf Stream separation is also improved, which leads to a reduction of the warm bias along the US East Coast from LR to VHR (Fig. 4). A paper on a dedicated analysis of the biases over the North Atlantic along the Gulf Stream is currently in preparation.

Farther north, the widespread cold bias up to about 6 K in LR is strongly reduced in HR, and even further in VHR, which is the configuration closest to observations (Fig. 4). The cold bias in LR is related to an unrealistically large sea ice extent, which covers the entire Labrador Sea and the western part of the subpolar North Atlantic (Figs. 7 and 8). The reduction of the cold bias between LR and VHR bias has a deep impact on the climate of the North Atlantic. In the atmosphere aloft, it improves the representation of the boreal winter (DJF) stormtrack (Fig. 9) and jet (Fig. 10). The boreal winter stormtrack is overestimated over the subpolar North Atlantic, particularly over the eastern part, in LR, likely related to an excessively strong meridional temperature gradient; by contrast, VHR stormtrack is much closer to ERA5 over the North Atlantic. In the ocean, excessive sea ice leads to a negative salinity bias above 2 psu in the subpolar North Atlantic in LR, which is much reduced in VHR (Fig. 11). Two mechanisms can explain this fresh bias in LR: on the one hand, a reduced oceanic salinity transport from subtropical latitudes by a weakened subpolar gyre (not shown); on the other, errors in the seasonal cycle of the sea ice, during which ice melting would cause an anomalous freshwater input in regions where it is not observed. The negative bias in surface salinity propagates into deeper levels, especially between 300 m and 1000 m in the Arctic (Fig. 12). Similarly, the warm subsurface bias at around 40 °N might also be related to the sea ice excess in the subpolar North Atlantic in LR (Fig. 11). Expanded sea ice in LR causes weaker subpolar gyre strength and associated northward heat transport (not shown), leading to heat accumulation in the intergyre region. However, although this bias is reduced at higher resolutions in HR and VHR, it is still present, suggesting other deficiencies in the formation of intermediate waters in the North Atlantic. The overly large sea ice cover also hampers oceanic deep mixing in the Labrador Sea in LR, whose main region of deep water formations are in the Nordic Seas instead (Fig. 13). Oceanic deep mixing takes larger values above 1000 m in VHR and HR in the Labrador Sea. A

409 detailed analysis of the characteristics and driving mechanisms of the deep water formation in
410 the Labrador Sea across the three resolutions and compared to observations is currently in
411 preparation.

412

413
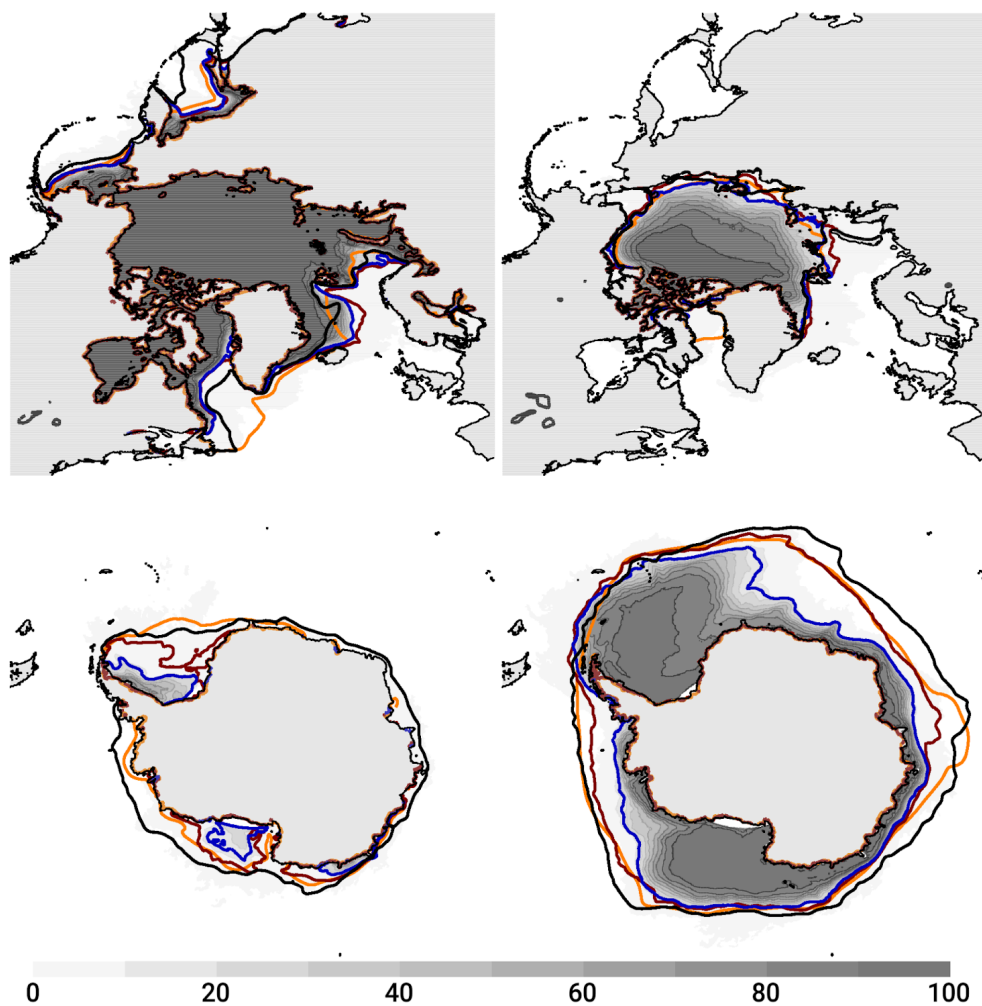
Figure 7. Sea ice concentration (in % of area) in the VHR model (gray shading) for the period
1980–2014. Contours are the 15-% value in the LR (orange), HR (red), and VHR (blue) models,
as well as in OSI SAF (black) for the period 1980–2014. Top/bottom panels are for the
Arctic/Antarctic in March (left) and September (right).

418
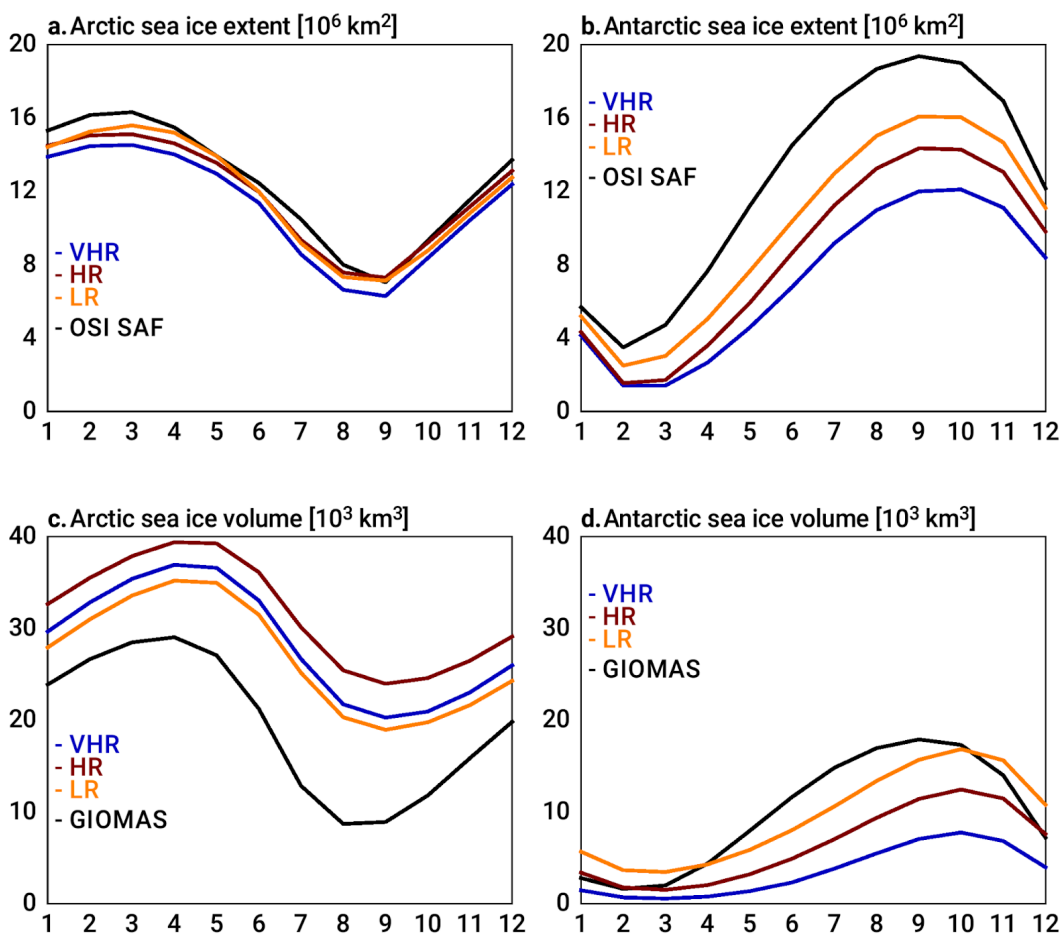
Figure 8. Monthly climatology in the sea ice extent (in 10^6 km²; top) and volume (in 10^3 km³; bottom) in the Arctic (left) and Antarctica (right) in the LR (yellow), HR (red), and VHR (blue) models, as well as in OSI SAF, for sea ice extent, and GIOMAS, for the volume, for the period 1980–2014.
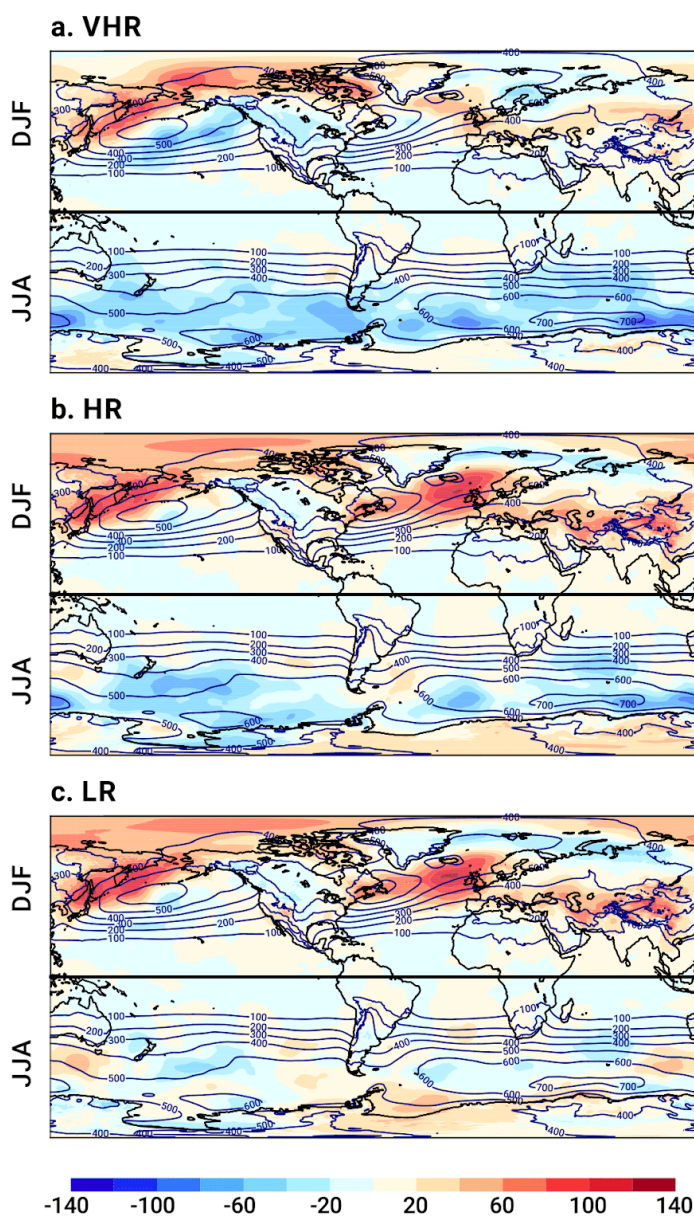
Figure 9. Bias in winter stormtrack, computed as the standard deviation of the 2–6 d band-pass filtered daily sea-level pressure (in Pa) with respect to ERA5 (contours in all the panels; in Pa) in the a) VHR, b) HR, and c) LR models for the period 1980–2014. Each panel show anomalies in the boreal winter (DJF; top) and austral winter (JJA; bottom)
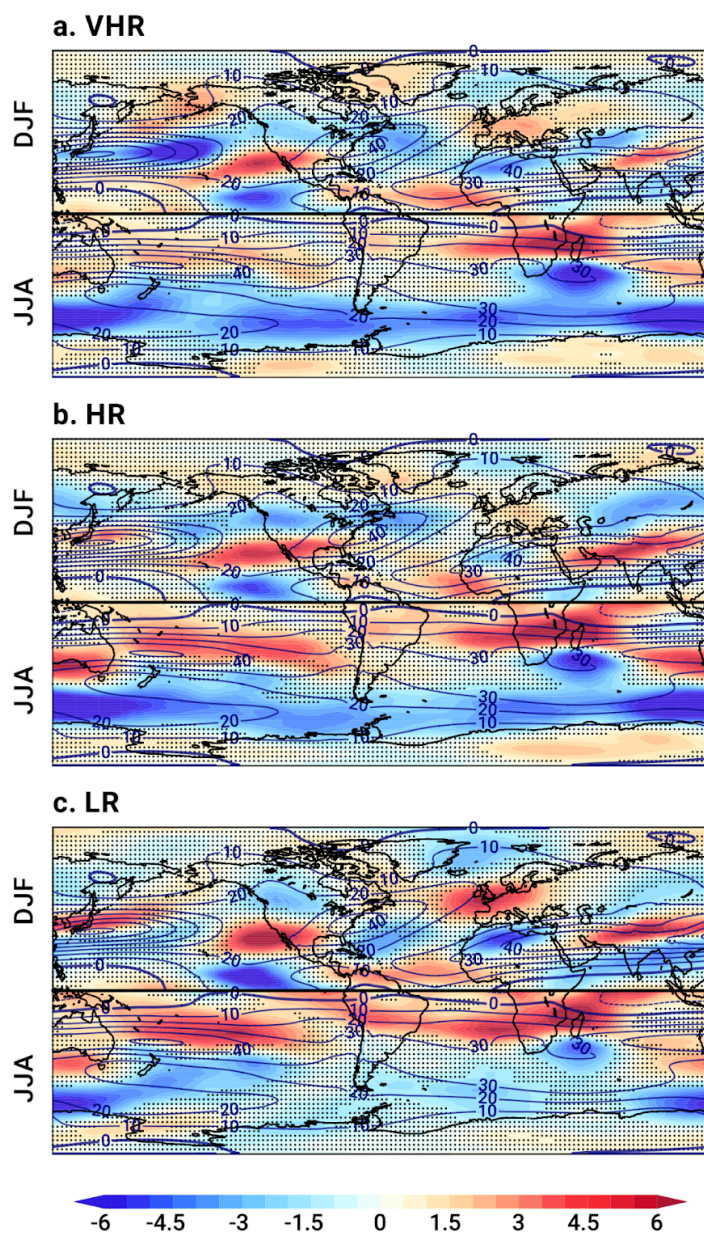
Figure 10. Bias in winter zonal wind at 250 hPa (in ms^{-1}) with respect to ERA5 (contours in all the panels; in ms^{-1}) in the a) VHR, b) HR, and c) LR models for the period 1980–2014. Stippling masks anomalies that are not significant at the 5 % level. Each panel show anomalies in the boreal winter (DJF; top) and austral winter (JJA; bottom)

a. VHR

b. HR

c. LR
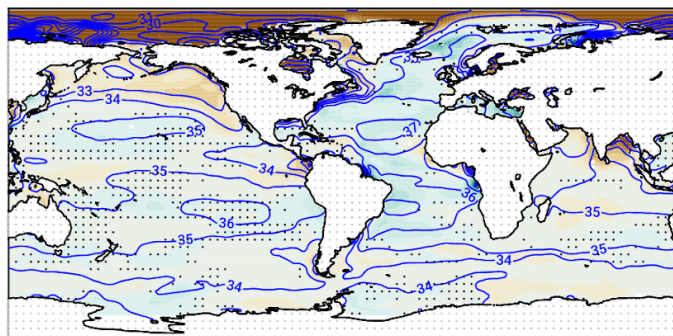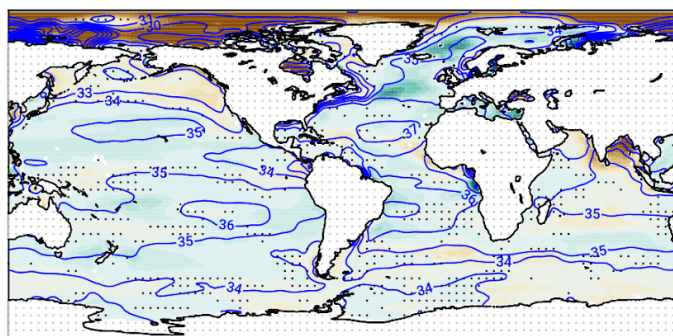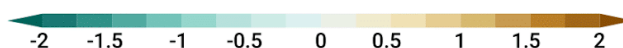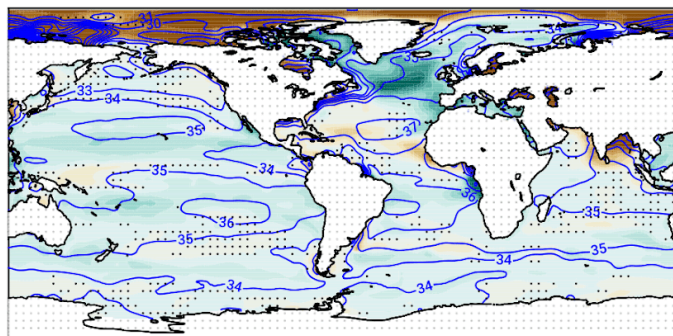
Figure 11. Sea-surface salinity bias (in psu) with respect to EN4 (contours in all the panels; in psu) in the a) VHR, b) HR, and c) LR models for the period 1980–2014. Stippling masks anomalies that are not significant at the 5 % level.
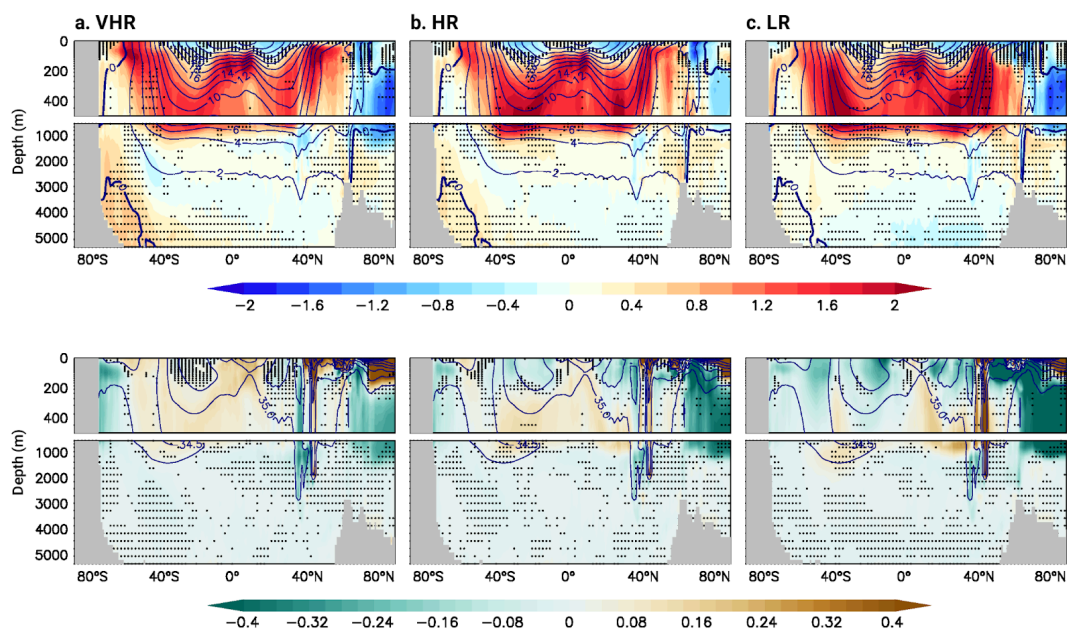
Figure 12. Bias in ocean potential temperature (in K; top) and in salinity (in psu; bottom) with respect to EN4 (contours in all the panels; in K, top, and psu, bottom) in the a) VHR, b) HR, and c) LR models for the period 1980–2014. Stippling masks anomalies that are not significant at the 5 % level. Each panel is separated into the upper and lower 500 m.
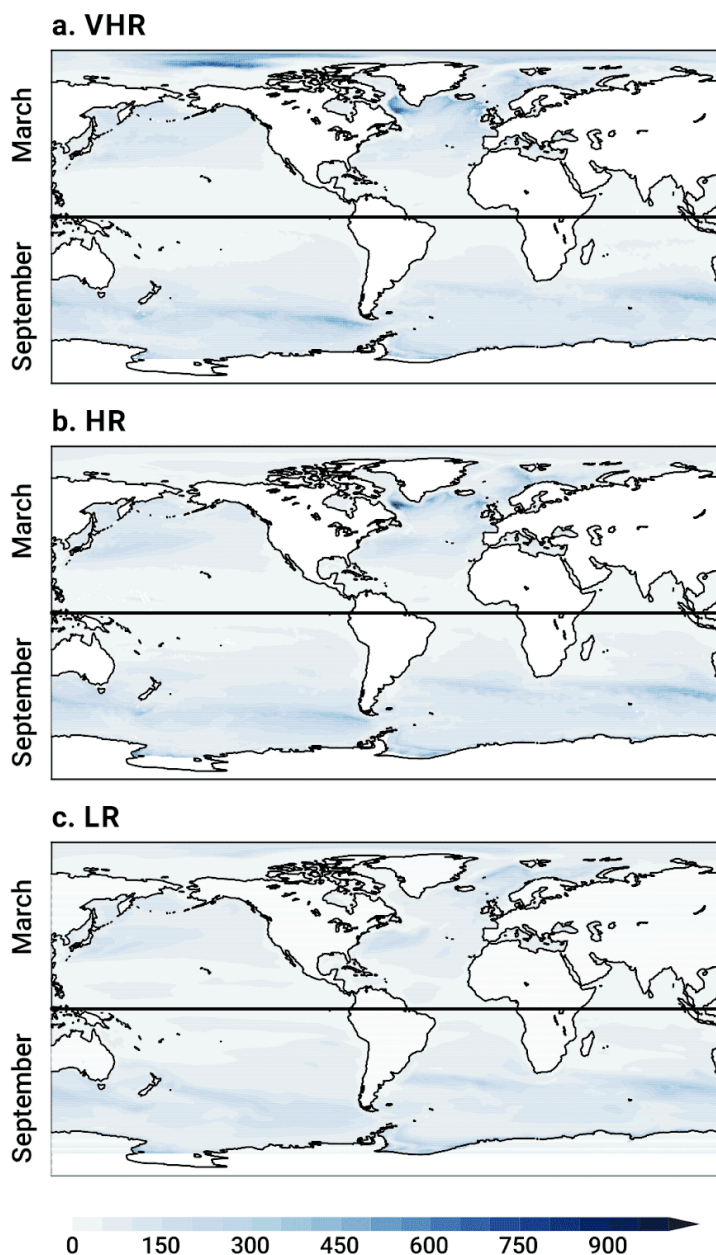
Figure 13. Mixed layer depth (in m) in the a) VHR, b) HR, and c) LR models for the period 1980–2014. Northern Hemisphere and Southern Hemisphere values are for March and September, respectively.

455 Weak deep mixing results in a relatively weak Atlantic Meridional Overturning Circulation
456 (AMOC; Fig. 14) in LR. The AMOC strength increases with resolution, related to the reduction
457 of the cold bias and sea ice extent bias over the subpolar North Atlantic. The strength of the
458 AMOC in VHR is thus the closest to the observed RAPID strength at 26 °N (17 ± 3 Sv;
459 Frajka-Williams et al., 2019) among the three models: 14 ± 3 Sv in VHR, 12 ± 4 Sv in HR, 11 ±
460 2 Sv in LR (computed from monthly streamfunction at 26 °N for the period 2004–2014). The
461 structure of the AMOC cell is similar in the three model configurations, with a main positive cell
462 in the upper 3000 m up to 60 °N and with a maximum at around 30 °N, and a negative deeper
463 one below with a strength of 2–4 Sv.

464
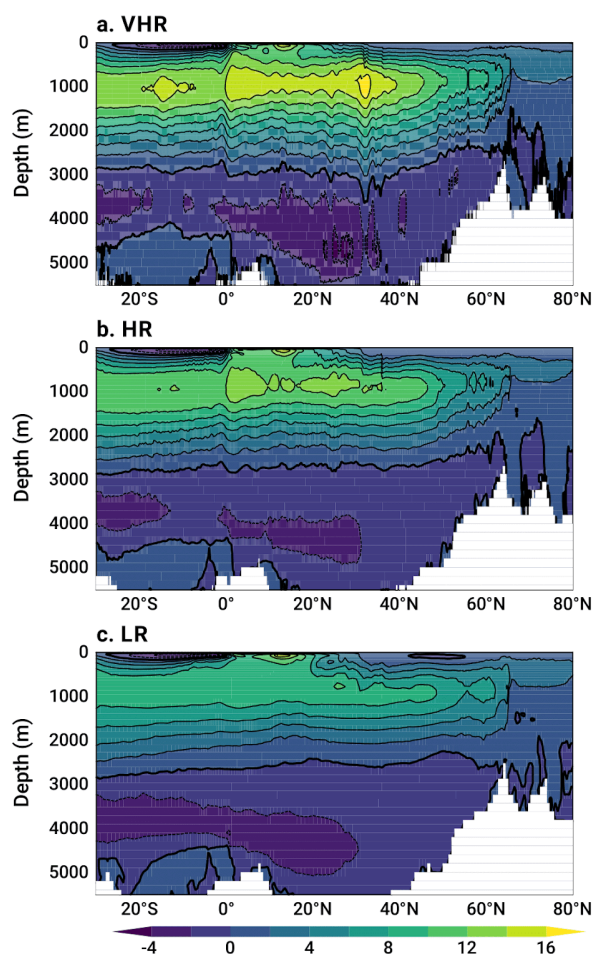
Figure 14. Atlantic overturning streamfunction (in Sv) in the a) VHR, b) HR, and c) LR models
466 for the period 1980–2014.

467   In HR, and even more in VHR, the cold bias over the Labrador Sea is replaced by a warm
468 bias (Fig. 4), up to 3–4 K in VHR. This bias also appears in other eddy-rich climate models,
469 related to a stronger Atlantic ocean heat transport than at lower resolutions (Roberts et al.,
470 2020b). Over the Nordic Seas, by contrast, a cold bias is present in the three models, although it
471 is somewhat reduced at VHR by 1–2 K compared to LR and HR (Fig. 4). In the three cases, this
472 bias is related to an excessively large sea ice cover in the region (Fig. 7). The warm bias over the
473 Labrador Sea and cold bias over the Nordic Seas in VHR might suggest a misrepresentation of
474 the distribution of oceanic heat transport between the two basins, favoring the westward transport
475 over the northward across-Ridge heat transport. It might also or instead be related to a
476 misrepresentation of the sea ice drift across the Denmark Strait (Gutjahr et al., 2022). Relatively
477 weak transport across the Strait would lead to ice deficit in the Labrador Sea, and hence
478 warming, and to ice accumulation in the Nordic Seas, hence cooling.

479   On a hemispheric scale, the three models simulate a slightly low Northern Hemisphere sea
480 ice extent, mainly due to the underestimation of the sea ice cover in the Sea of Okhotsk, Baltic
481 Sea, and Labrador Sea in HR and VHR (Fig. 8). By contrast, the three models show an overly
482 large sea ice volume by about 10^4 km^3 compared to GIOMAS (Fig. 9), as they all simulate very
483 thick sea ice in the central Arctic (not shown). Anomalously thick ice in the models leads to an
484 excess of brine rejection (not shown), which can explain the positive salinity bias above 2 psu in
485 the upper 100–200 m of the Arctic Ocean (Figs. 11 and 12). In VHR, the associated increase in
486 upper-ocean density leads to deeper oceanic mixing than in LR or HR, with a mixed layer depth
487 in the central Arctic that can reach up to 1000 m (Fig. 13).

488   Over the Pacific, biases tend to be weaker than over the Atlantic. A warm bias of about 1 K
489 develops over the subpolar North Pacific from LR to VHR (Fig. 4), which could explain the
490 negative bias in boreal winter (DJF) stormtrack aloft (Fig. 9) and the weaker jet stream over the
491 central Pacific in VHR (Fig. 10).

492   Over land, the cold bias over the Sahara is reduced with increased resolution (Fig. 4).
493 Similarly, the cold biases over large mountain ranges, such as the Rockies, the Andes, and the
494 Himalaya, up to about several degrees in LR are much reduced in VHR, related to better resolved
495 orography.

496

497

3.4. Southern Ocean

The Southern Ocean is the region where VHR performs the worst compared to HR and LR. The warm bias over the Southern Ocean increases with resolution, up to 4–5 K in VHR, compared to 1–2 K and 2–3 K for HR and LR respectively (Fig. 4). It tends to be largest over the Atlantic and Indian sectors of the Southern Ocean and close to the Antarctic coast. Although the warm bias remains generally confined to the upper 100–200 m at around 60 °S, it might also be connected to the warm bias at depth between 2000 m and 4000 m (Fig. 12).

Two main mechanisms could explain the Southern Ocean warm bias: VHR has the largest cloud cover underestimation of the three models, especially over the Atlantic and Indian sectors, up to 15 % in VHR compared to 5–10 % in LR and HR (Fig. 5). Previous studies have related the Southern Ocean warm biases to misrepresentation and underestimation of the mixed-phase clouds, which lead to an excess of shortwave radiation reaching the surface, thereby warming it (e.g., Hwang, and Frierson, 2013; Hyder et al., 2018). Connected to the warm bias, VHR also shows the lowest sea ice extent of the three resolutions all year round (Figs. 7 and 8). Although the three models underestimate the Antarctic sea ice extent, in VHR this is nearly half as in observations for the same period (OSI SAF, 1980–2014). In terms of sea ice volume (Fig. 8), however, LR shows larger values by about $2 \cdot 10^3$ km^3 than GIOMAS between November and April, pointing to overly thick sea ice. As for the extent, VHR also shows the lowest sea ice volume, nearly half of the values in GIOMAS. The three models show the maximum volume one month later than in GIOMAS, in October rather than in September. This contrasts with the Arctic, where the three models capture the general shape of the seasonal cycle.

The surface warming over the Southern Ocean leads to a widespread underestimation of the stormtracks (Fig. 9) and jet stream (Fig. 10) in the austral winter (JJA) in HR and, especially, in VHR, compared to LR, which is much closer to ERA5. Although precipitation is also underestimated over the Southern Ocean, specially in VHR, this is not a particularly strong bias, at least compared to those over the tropical regions (Fig. 6).

Late austral summer (September) deep mixing tends to increase by about 200 m from LR to HR and VHR, especially in the Pacific sector. These two latter resolutions show similar deep mixing mean state, with variations only due to resolution and the better representation of the mesoscale in VHR (Fig. 13). The underestimation of the stormtrack over the Southern Ocean therefore does not seem to have an impact on the oceanic mixing below in VHR.

3.5 Air–sea coupling

We compare the change in the intensity of air–sea coupling from LR to VHR via the computation of cross-correlation coefficients of the deseasonalized monthly SST and net surface energy flux (Fig. 15). This analysis has extensively been used to study regions in which the ocean tends to drive atmospheric variability (correlation coefficient values approaching one) or vice versa (correlation coefficient values close to zero; e.g., Bishop et al., 2017; Small et al., 2019). The three model configurations are compared with the ERA5 reanalysis, as done in the previous Sections for the biases. To complement the analysis with a non-model based product, we also include satellite observations of radiative fluxes from J-OFURO3 (Tomita et al., 2019). The two products show an overall good agreement, with areas of large correlation coefficient values at the Equator, along the western boundary currents, and over the Southern Ocean (Fig. 15a,b). These areas, nonetheless, tend to be broader in J-OFURO3 than in ERA5.

Over the tropics, the three configurations tend to underestimate the coupling around the Equator, although they all reproduce well the band of correlation coefficients of high values along the equatorial Pacific and Atlantic. However, this band is narrower in LR and HR over the subtropics than it is in ERA5 and J-OFURO3. VHR is thus the closest configuration to the two reference observational products in the region. This result highlights the need for a model resolution finer than 25 km in both the ocean and atmosphere to represent realistic tropical climate interactions, in agreement with conclusions in Section 3.2.

At mid-latitudes, the coupling is greatly improved in HR and VHR compared to LR, particularly over the subpolar regions compared to ERA5 and J-OFURO3. LR shows a rather smooth pattern, with very low values in key regions over the Gulf Stream, Kuroshio Current, and Southern Ocean, which suggests a standard 1° resolution is insufficient to represent a realistic air–sea coupling. VHR and HR show, by contrast, sharper gradients in the correlation coefficient values close to 1 over those regions. This result is consistent with previous studies, which also found a degradation of the air–sea coupling in coarse grids, especially above 1° (e.g., Small et al., 2019). However, VHR shows unrealistic broader areas of higher correlation coefficient values than ERA5 and J-OFURO3 at mid-latitudes, degrading results from HR. One hypothesis for this discrepancy might result from the difference of IFS grid resolution between VHR (T1279) and ERA5 (T639), since the relationship between SST and turbulent fluxes shows certain scale dependency (e.g., Small et al., 2019; Sun and Wu, 2022). However, results do not

560 improve even when regridding VHR onto ERA5 grid before computing the correlation
561 coefficients (not shown). A second hypothesis is the lack of the ocean current feedback in VHR,
562 hence the lack of eddy-killing, which can control the simulated Gulf Stream's dynamics and
563 energy pathways (Renault et al., 2023). However, the pattern of correlation coefficient values
564 remains relatively unchanged when it is computed with a VHR configuration that includes a
565 parameterization that considers the wind adjustment to the ocean current feedback (not shown)
566 (Renault et al., 2019). The results suggest that the VHR's ocean exerts a stronger and more
567 widespread influence on the atmosphere variability than in HR and LR.

568   Further north, air–sea coupling is overestimated in all the models over the Nordic Seas, likely
569 related to the excess in sea ice in the region and its changes over the seasonal cycle. Together, the
570 results suggest that a realistic air–sea coupling requires grids finer than 1/4° at least, with
571 potential local improvements on a 1/12° grid, especially over the Tropics.

572

573 **4. Discussion and Conclusions**

574 This paper presents the eddy-rich configuration of the EC-Earth3P-VHR global model for
575 HighResMIP. We describe both the necessary technical developments to run the model
576 efficiently, and the main features of the simulated climate compared to recent observations
577 (1980–2014 period) and to two lower-resolution model configurations (the eddy-present,
578 ~25-km-grid EC-Earth3P-HR; and the non-eddy, ~100-km-grid EC-Earth3P-LR). The
579 EC-Earth3P-VHR (or VHR) uses a comparable atmospheric and oceanic resolution of 10–15 km
580 in a global fully coupled setup, which is, to our knowledge, one of the finest combined grids ever
581 used to date to perform long climate integrations for CMIP. Our focus here is on the
582 HighResMIP historical simulation (HighResMIP's hist-1950). This run is part of a larger set of
583 runs, which includes a spin-up and control runs (HighResMIP's control-1950), a future extension
584 under the ssp8.5 scenario (HighResMIP's highres-future), three hosing simulations forced by
585 idealized Greenland melting, and AMIP sensitivity simulations, all performed within the
586 European PRIMAVERA project and the Spanish STREAM project. Those additional simulations
587 will be described in their corresponding publications, which are currently in preparation.
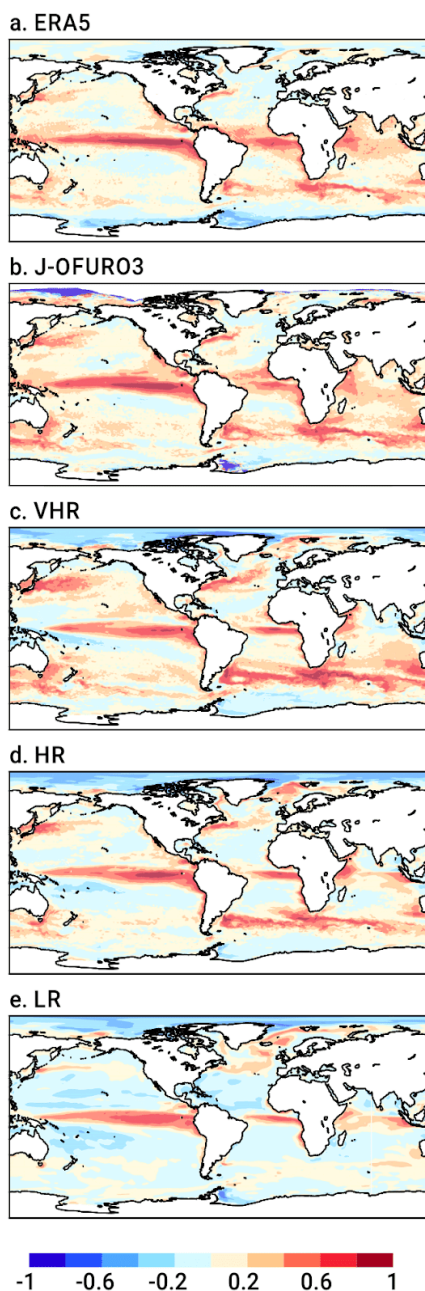
Figure 15. Cross-correlation coefficients between monthly SST and net surface energy flux for the period 1980–2014 in a) ERA5, b) J-OFURO3, and in the c) VHR, d) HR, and e) LR models. The seasonal cycle and linear trends are removed from the monthly SSTs and energy fluxes before the correlation coefficients are computed. This is done on the original grid in all the cases.

The comparison across the three resolutions (this is, VHR, HR, and LR), all with the same physics and no additional tuning, allows identifying regions where increased resolution improves the model performance with respect to observations. One of those regions is the Tropics, and specially the equatorial Pacific, where the cold tongue bias and the dry bias above are both reduced in VHR compared to HR and LR. Wengel et al. (2021) also reports a similar bias reduction in an eddy-resolving configuration of the CESM (0.25° resolution in the atmosphere, 0.1° resolution in the ocean), which they link to better represented mesoscale features, such as tropical instability waves. Similarly, the HadGEM3-GC3.1 global model shows a reduced dry bias over the equatorial Pacific in its configuration with a 1/12° ocean and a 50-km atmosphere (Roberts et al., 2019). By contrast, the eddy-rich MPI-ESM1.2-ER global model (1/12° ocean as well) shows no evident changes in equatorial precipitation when coupled to a 100-km atmosphere (Gutjahr et al., 2019). Combined, these results suggest that resolutions finer than 25–50 km might be needed in both the atmosphere and ocean to improve surface coupling and reduce biases. However, minimizing equatorial precipitation biases might actually be much more complex than simply increasing model resolution, as found for the ICON global atmosphere–ocean model with a uniform grid spacing of 5 km. Despite its high atmosphere and ocean resolutions, this model still exhibits a strong dry bias over the equatorial Pacific driven by a surface cold bias underneath (Hohenegger et al., 2022; Segura et al., 2022). This model, however, is not directly comparable to those other HighResMIP models, as it includes a minimum set of parametrization. Thus, while convection is directly resolved in ICON, it is parametrized in VHR and the listed models. The incorrect representation of the equatorial SST structure in ICON might instead be related to unresolved sub-grid processes (Segura et al., 2022).

The Gulf Stream is another region in which increased model resolution is beneficial, with a reduced temperature biases over the separation region and the central North Atlantic in VHR compared to HR and LR. Such improvements have been related to the resolving of the first baroclinic Rossby radius of deformation over most of the region and/or the exceeding of a critical Reynolds number (e.g., Chassignet and Marshall, 2008). Similar results have also been reported for the HadGEM3-GC3.1 (Roberts et al., 2019) and MPI-ESM1.2-ER (Gutjahr et al., 2019) global models, both with a 1/12° oceanic grid but coarser atmospheric grids (~50 km and ~100 km, respectively). This suggests that oceanic resolution is a critical factor for the Gulf

624 Stream representation. Nonetheless, other model features might also be relevant to simulate a
625 realistic Gulf Stream, as no improvement is found in the CESM1.3 model between a 1°- and a
626 0.1°- oceanic grid, for which the Gulf Stream separation occurs too far north (Chang et al.,
627 2020). One of the many potential reasons behind the discrepancy might be the obvious difference
628 in the number of atmospheric vertical levels: 91 in VHR, 85 in HadGEM3-GC3.1 (Roberts et al.,
629 2019), 95 in MPI-ESM1.2-ER (Gutjahr et al., 2019), but only 30 in CESM1.3 (Meehl et al.,
630 2019), which is expected to degrade the representation of key stratosphere–troposphere
631 interactions affecting North Atlantic variability, and, by extension, the wind field, which is
632 critical for the Gulf Stream separation. As nicely summarized in Chassignet and Marshall (2008),
633 however: "The Gulf Stream separation, indeed, turns out to be quite sensitive to a variety of
634 other factors such as subgrid scale parametrization, subpolar gyre strength and water mass
635 properties, [deep western boundary current] strength, representation of topography, and the
636 choice of model grid". A realistic representation of the Gulf Stream is crucial for the North
637 Atlantic and European climate. SST biases in the Gulf Stream can drive not only local changes
638 over the North Atlantic, but a large-scale dynamic response over remote regions of the Northern
639 Hemisphere through a quasi-zonal planetary barotropic Rossby wave response (Lee et al., 2018).
640 Similarly, a more realistic, farther-south Gulf Stream has been shown to shift north in
641 simulations with increased CO_2 in models at eddy-rich resolutions (Saba et al., 2016;
642 Moreno-Chamarro et al., 2021). This shift would lead to amplified warming of the US East
643 coastal region, which might be consistent with the anomalous warming observed in the Gulf
644 Stream area in recent decades (Pershing et al., 2015; Todd and Ren, 2023). Reducing biases in
645 the Gulf Stream area is therefore key to reproducing a realistic atmospheric circulation and to the
646 sensitivity of the response to an external forcing.

647 Mainly related to increased atmospheric resolution, VHR also shows reduced precipitation
648 biases over mountain ranges all over the world. This suggests VHR might provide more realistic
649 regional information of precipitation variability and future changes than lower resolution models
650 can. Giorgi et al. (2016), in fact, showed that increased model resolution leads to stronger
651 summer precipitation changes over the Alpine region, using climate change projections with a
652 regional atmospheric model of ~12-km grid. VHR uses a similar resolution but on a global scale,
653 without the need to be constrained by lower resolution models.

654   On the negative side, we find that increased model resolution alone can be insufficient to
655 reduce important and well-known biases in the climate or even cause model degradation in VHR.
656 The warm bias over the coastal tropical upwelling areas, the Southern Ocean warm bias, and the
657 rainfall excess bias over warm tropical waters all persist or even increase in VHR compared to
658 HR and LR. These biases point to deficiencies in the model physics, specially in the atmosphere,
659 and more particularly, in the cloud parameterizations. In VHR, both the warm bias over eastern
660 tropical upwelling areas and the Southern Ocean are connected to negative biases in cloud cover.
661 This reinforces the established idea that insufficient stratocumulus decks over the upwelling
662 areas (e.g., Richter, 2015) and mixed-phase clouds over the Southern Ocean (e.g., Hyder et al.,
663 2018) play key roles in setting up those biases. Cloud biases can be particularly insensitive to
664 increases in model resolution, both in the ocean and atmosphere, from ~100-km grids to
665 25–50-km grids (Moreno-Chamarro et al., 2022). Yet, for example, improved cloud
666 microphysics closer to observations have been shown to help reduce shortwave radiation biases
667 over the Southern Ocean in the Met Office's Unified Model (Varma et al., 2020). Reducing these
668 biases as much as possible is critical, since they can have wider, global impacts on the climate,
669 driving, for example, additional biases in tropical precipitation through the effect on the global
670 energy budget (e.g., Hwang et al., 2013; Hawcroft et al., 2017).

671   It is interesting to note, nonetheless, that although LR, HR, and VHR all share the same cloud
672 scheme, it is VHR that develops the strongest Southern Ocean bias. This might be related to the
673 lack of additional model tuning from LR to HR and VHR. Rackow et al. (2024) showed that
674 tuning the top-of-the-atmosphere radiation contributed to reducing the warming excess over the
675 Southern Ocean in the IFS-FESOM global model at ~5-km resolution. The HighResMIP
676 protocol suggests that no tuning is performed across resolutions to ensure any changes in the
677 simulated climate can solely be attributed to changes in resolution (Haarsma et al., 2016). This
678 approach can lead to undesired model degradation: for example, the untuned, low-resolution
679 ECMWF model for HighResMIP shows an overly weak AMOC and a large cold bias over the
680 North Atlantic compared to its well-tuned, high-resolution counterpart (Roberts C.D. et al.,
681 2018). This can hinder model comparison and a clean understanding of the effect of model
682 resolution, as biases can have large-scale climatic impacts (e.g., Hwang et al., 2013; Hawcroft et
683 al., 2017; Lee et al., 2018) and affect the response sensitivity to forcing (e.g., McGee et al.,
684 2018).

685   With respect to the spin-up, the HighResMIP protocol suggests a 50-year period (Haarsma et
686 al., 2016). For all the configurations, this period is insufficient to equilibrate the full ocean,
687 although the upper 1000 m equilibrates faster than the lower-part, and VHR does it faster and
688 appears more stable after 100 years than HR and LR. The eddy-rich HadGEM3-GC3.1 also
689 shows smaller drifts at the end of the 50-year period than its lowest resolution versions (Roberts
690 et al., 2019). By contrast, for the CESM1.3 model, the low and high-resolution configurations
691 only show a more stable climate after 150 years, related to a strong top-of-the-atmosphere energy
692 imbalance (Chang et al., 2020). This led the authors to propose "150 to 200 years of model
693 spin-up as a future strategy for initializing HR climate model simulations" (Chang et al., 2020).
694 However, considering how computationally expensive these simulations are, new techniques
695 might need to be introduced to tune and spin these models up faster and for longer. As much as
696 tuning can still be "artisanal in character" at many research centers (Mauritsen et al., 2012), new
697 and faster methods are being implemented to speed up the exploration of the space of parameters
698 to find the best fit with observations. These methods include for example machine learning
699 (Hourdin et al., 2021), simplified configurations (Wan et al., 2014) , adjoints (Lyu et al., 2018),
700 or model emulators (Williamson et al., 2013). Additional techniques have also been proposed to
701 spin models up faster at much less computational costs; these include using for example
702 Newton-Krylov methods (Bernsen et al., 2008; Merlis and Khatiwala, 2008), or replacing the
703 atmosphere model by model data (Lofverstrom et al., 2020). Implementing similar techniques in
704 future HR and VHR simulations would help accelerate both the spin-up and tuning phases.

705   To summarize, we here present the eddy-rich version of the EC-Earth global climate model,
706 EC-Earth3P-VHR, with atmospheric and oceanic resolutions of 10–15 km. The analysis of its
707 main climate features reveals improvements with respect to two lower resolution versions, such
708 as a reduced dry equatorial bias over the Pacific, a more realistic Gulf Stream representation, and
709 more accurate rainfall over mountain areas. Other biases persist or degrade, such as the warm
710 biases over the subtropical upwelling regions and Southern Ocean, or the tropical precipitation
711 excess. VHR's global resolution is at a similar level of many regional models, such as those
712 participating in CORDEX, and it is much finer than most of the standard CMIP models. This
713 opens a window of opportunity for model comparison and evaluation, as well as process
714 understanding of much more realistic present-day and future climate and on a more regional
715 scale.

716

Code and Data Availability

718 The data of the EC-Earth3P-LR and -HR models are available from ESGF
719 (https://esgf-index1.ceda.ac.uk/search/cmip6-ceda/, last access: 20 June 2024) via the references
720 provided in Section 2.3: EC-Earth3P (https://doi.org/10.22033/ESGF/CMIP6.4683, EC-Earth,
721 2018; https://doi.org/10.22033/ESGF/CMIP6.4682, EC-Earth, 2019). Data of ERA-5 are freely
722 available at https://www.ecmwf.int/en/forecasts/dataset/ecmwf-reanalysis-v5 (Hersbach et al.,
723 2020; https://doi.org/10.24381/cds.6860a573, Hersbach et al., 2019), while GPCP data are at
724 https://psl.noaa.gov/data/gridded/data.gpcp.html (Adler et al., 2003), ESA cloud cover data are at
725 https://climate.esa.int/en/projects/cloud/data/ (Stengel et al., 2020), EN4 data version 4.2.2 are at
726 https://www.metoffice.gov.uk/hadobs/en4/ (Good et al., 2013), OSI SAF (OSI-409/OSI-409-a)
727 sea ice concentration data are at https://osi-saf.eumetsat.int/products/sea-ice-products
728 (EUMETSAT Ocean and Sea Ice Satellite Application Facility, 2015), GIOMAS sea ice volume
729 data are at https://psc.apl.washington.edu/zhang/Global_seaice/data.html (Zhang and Rothrock,
730 2003), and J-OFURO3 flux data are at https://www.j-ofuro.com/en/dataset/ (Tomita et al., 2019).
731 The model data and plot scripts to reproduce the figures can be obtained from
732 https://zenodo.org/records/12078052 (Moreno-Chamarro, 2024). The model code developed at
733 ECMWF, including IFS and the Finite Volume Module (FVM), is intellectual property of
734 ECMWF and its member states. Permission to access the EC-Earth source code can be requested
735 from the EC-Earth community via the EC-Earth website (http://www.ec-earth.org/, last access:
736 July 2024) and may be granted, if a corresponding software license agreement is signed with
737 ECMWF. The repository tag for the version of IFS and EC-Earth3P-VHR used in this work is
738 3.2.2 (see Section 2.1) and is available through r8643. The EC-Earth workflow software used to
739 run the simulations at the BSC is stored and version controlled in the BSC Earth Sciences GitLab
740 repository (https://earth.bsc.es/gitlab/es/auto-ecearth3, last access: July 2024). Permission to
741 access the repository can be requested from the Earth Sciences Department at the BSC and may
742 be granted if the applicant has access to the EC-Earth code and the BSC HPC infrastructure. The
743 workflow management system for running the simulations is distributed under Apache License
744 2.0 as a public project (https://earth.bsc.es/gitlab/es/autosubmit, last access: July 2024) in the
745 BSC GitLab repository.

746

Author Contributions

TA, MA, MC, EF, and SP developed the model setup. EMC and TA ran the simulations. PAB and DK post-processed and cmorized the model data. EMC analyzed the data and wrote the manuscript with input from all the authors.

Competing interests

The authors declare that they have no conflict of interest.

References

Abdalla, S., Isaksen, L., Janssen, P. A. E. M., and Nils, W.: Effective spectral resolution of ECMWF atmospheric forecast models, ECMWF Newsletter No. 137, 19–22, https://doi.org/10.21957/rue4o7ac, 2013.

Acosta, M.C., Palomas, S. and Tourigny, E.: Balancing EC-Earth3 Improving the Performance of EC-Earth CMIP6 Configurations by Minimizing the Coupling Cost. Earth and Space Science, 10(8), p.e2023EA002912, https://doi.org/10.1029/2023EA002912, 2023.

Acosta, M. C., Palomas, S., Paronuzzi Ticco, S. V., Utrera, G., Biercamp, J., Bretonniere, P.-A., Budich, R., Castrillo, M., Caubel, A., Doblas-Reyes, F., Epicoco, I., Fladrich, U., Joussaume, S., Kumar Gupta, A., Lawrence, B., Le Sager, P., Lister, G., Moine, M.-P., Rioual, J.-C., Valcke, S., Zadeh, N., and Balaji, V.: The computational and energy cost of simulation and storage for climate science: lessons from CMIP6, Geosci. Model Dev., 17, 3081–3098, https://doi.org/10.5194/gmd-17-3081-2024, 2024.

778 Adler, R. F., Huffman, G. J., Chang, A., Ferraro, R., Xie, P. P., Janowiak, J., Rudolf, B.,
779   Schneider, U., Curtis, S., Bolvin, D., and Gruber, A.: The version-2 global precipitation
780   climatology project (GPCP) monthly precipitation analysis (1979–present), J.
781   Hydrometeorol.,   4,   1147–1167,
782   https://doi.org/10.1175/1525-7541(2003)004<1147:TVGPCP>2.0.CO;2,   2003   (data
783   available at: https://psl.noaa.gov/data/gridded/data.gpcp.html, last access: 30 March 2023).

784 Amante, C. and Eakins, B.W.: ETOPO1 arc-minute global relief model: procedures, data
785   sources and analysis, 2009.

786 Baker, A.J., Schiemann, R., Hodges, K.I., Demory, M. E., Mizielinski, M. S., Roberts, M. J.,
787   Shaffrey, L. C., Strachan, J. and Vidale, P. L.: Enhanced climate change response of
788   wintertime North Atlantic circulation, cyclonic activity, and precipitation in a
789   25-km-resolution global atmospheric model. Journal of Climate, 32(22), 7763–7781,
790   https://doi.org/10.1175/JCLI-D-19-0054.1, 2019.

791 Balsamo, G., Beljaars, A., Scipal, K., Viterbo, P., van den Hurk,B., Hirschi, M., and Betts, A.
792   K.: A revised hydrology for theECMWF model: Verification from field site to terrestrial
793   waterstorage and impact in the Integrated Forecast System, J. Hydrometeorol., 10, 623–643,
794   2009.

795 Becker, J.J., Sandwell, D.T., Smith, W.H.F., Braud, J., Binder, B., Depner, J.L., Fabre, D.,
796   Factor, J., Ingalls, S., Kim, S.H. and Ladner, R.: Global bathymetry and elevation data at 30
797   arc   seconds   resolution: SRTM30_PLUS.   Marine   Geodesy,   32(4),   355–371,
798   https://doi.org/10.1080/01490410903297766, 2009.

799 Bellucci, A., Athanasiadis, P. J., Scoccimarro, E., Ruggieri, P., Gualdi, S., Fedele, G.,
800   Haarsma, R. J., Garcia-Serrano, J., Castrillo, M., Putrahasan, D., and Sanchez-Gomez, E.:
801   Air-Sea interaction over the Gulf Stream in an ensemble of HighResMIP present climate
802   simulations, Clim. Dynam., 56, 2093–2111, https://doi.org/10.1007/s00382-020-05573-z,
803   2021.

804 Bernsen, E., Dijkstra, H.A., Thies, J. and Wubs, F.W.: The application of Jacobian-free
805   Newton–Krylov methods to reduce the spin-up time of ocean general circulation models.
806   Journal   of   Computational   Physics,   229(21),   8167–8179,
807   https://doi.org/10.1016/j.jcp.2010.07.015, 2010.

808 Biastoch, A., Schwarzkopf, F. U., Getzlaff, K., Rühs, S., Martin, T., Scheinert, M., Schulzki,
809 T., Handmann, P., Hummels, R. and Böning, C. W.: Regional imprints of changes in the
810 Atlantic Meridional Overturning Circulation in the eddy-rich ocean model VIKING20X.
811 Ocean Science, 17(5), 1177–1211, https://doi.org/10.5194/os-17-1177-2021, 2021.

812 Bishop, S. P., Small, R. J., Bryan, F. O. and Tomas, R. A.: Scale dependence of midlatitude
813 air–sea interaction. Journal of Climate, 30(20), 8207–8221,
814 https://doi.org/10.1175/JCLI-D-17-0159.1, 2017.

815 Chassignet, E. and Marshall, D.: Gulf Stream separation in numerical ocean models.
816 Geophysical Monograph Series, 177, https://doi.org/10.1029/177GM05, 2008.

817 Craig, A., Valcke, S., and Coquart, L.: Development and performance of a new version of the
818 OASIS coupler, OASIS3-MCT_3.0, Geosci. Model Dev., 10, 3297–3308,
819 https://doi.org/10.5194/gmd-10-3297-2017, 2017.

820 Czaja, A., Frankignoul, C., Minobe, S. and Vannière, B.: Simulating the midlatitude
821 atmospheric circulation: what might we gain from high-resolution modeling of air-sea
822 interactions?. Current climate change reports, 5, 390–406,
823 https://doi.org/10.1007/s40641-019-00148-5, 2019

824 Doi, T., Vecchi, G. A., Rosati, A. J., and Delworth, T. L.: Biases in the Atlantic ITCZ in
825 seasonal–interannual variations for a coarse-and a high-resolution coupled climate model, J.
826 Climate, 25, 5494–5511, https://doi.org/10.1175/JCLI-D-11-00360.1, 2012.

827 EC-Earth Consortium (EC-Earth): EC-Earth-Consortium EC-Earth3P-HR model output
828 prepared for CMIP6 HighResMIP hist-1950, Earth System Grid Federation [data set; last
829 access: 18 May 2023], https://doi.org/10.22033/ESGF/CMIP6.4683, 2018.

830 EC-Earth Consortium (EC-Earth): EC-Earth-Consortium EC-Earth3P model output prepared
831 for CMIP6 HighResMIP hist-1950, Earth System Grid Federation [data set; last access: 18
832 May 2023], https://doi.org/10.22033/ESGF/CMIP6.4682, 2019.

833 EUMETSAT Ocean and Sea Ice Satellite Application Facility: Global sea ice concentration
834 reprocessing dataset 1978–2015 (v1.2), Norwegian and Danish Meteorological Institutes,
835 available at: https://catalogue.ceda.ac.uk/uuid/8bbde1a8a0ce4a86904a3d7b2b917955 (last
836 access: 8 February 2019), 2015.

837 Frajka-Williams, E., Ansorge, I.J., Baehr, J., Bryden, H.L., Chidichimo, M.P., Cunningham,
838 S.A., Danabasoglu, G., Dong, S., Donohue, K.A., Elipot, S. Heimbach, P., Holliday, N.P.,

839   Hummels, R., Jackson, L.C., Karstensen, J., Lankhorst, M., Le Bras, I.A., Lozier, M. S.,
840   McDonagh, E.L., Meinen, C.S., Mercier, H., Moat, B.I., Perez, R.C., Piecuch, C.G., Rhein,
841   M., Srokosz, M.A., Trenberth, K.E., Bacon, S., Forget, G., Goni, G., Kieke, D., Koelling, J.,
842   Lamont, T., McCarthy, G.D., Mertens, C., Send, U.,Smeed, D.A., Speich, S., van den Berg,
843   M.,Volkov,D., Wilson, C.: Atlantic Meridional Overturning Circulation: Observed Transport
844   and Variability, Frontiers in Marine Science, 6, https://doi.org/10.3389/fmars.2019.00260,
845   2019.
846   Giorgi, F., Torma, C., Coppola, E., Ban, N., Schär, C. and Somot, S.: Enhanced summer
847   convective rainfall at Alpine high elevations in response to climate warming. Nature
848   Geoscience, 9(8), 584-589, https://doi.org/10.1038/ngeo2761, 2016.
849   Good, S. A., M. J. Martin, M. J., and Rayner, N. A.: EN4: quality controlled ocean
850   temperature and salinity profiles and monthly objective analyses with uncertainty estimates,
851   Journal   of   Geophysical   Research: Oceans,   118,   6704-6716,
852   https://doi.org/10.1002/2013JC009067,   2013   (data   available   at:
853   https://www.metoffice.gov.uk/hadobs/en4/, last access: 12 November 2021).
854   Gutjahr, O., Jungclaus, J. H., Brüggemann, N., Haak, H. and Marotzke, J.: Air-sea interactions
855   and water mass transformation during a katabatic storm in the irminger sea. Journal of
856   Geophysical   Research: Oceans,   127(5),
857   e2021JC018075,https://doi.org/10.1029/2021JC018075, 2022.
858   Gutjahr, O., Putrasahan, D., Lohmann, K., Jungclaus, J.H., von Storch, J.S., Brüggemann, N.,
859   Haak, H. and Stössel, A.: Max Planck Institute earth system model (MPI-ESM1.2) for the
860   high-resolution model intercomparison project (HighResMIP). Geoscientific Model
861   Development, 12(7), 3241–3281, https://doi.org/10.5194/gmd-12-3241-2019, 2019.
862   Haarsma, R., Acosta, M., Bakhshi, R., Bretonnière, P. A., Caron, L. P., Castrillo, M., Corti, S.,
863   Davini, P., Exarchou, E., Fabiano, F. and Fladrich, U.: HighResMIP versions of EC-Earth:
864   EC-Earth3P and EC-Earth3P-HR–description, model computational performance and basic
865   validation.   Geoscientific   Model   Development,   13(8),   3507–3527,
866   https://doi.org/10.5194/gmd-13-3507-2020, 2020.
867   Haarsma, R. J., Roberts, M. J., Vidale, P. L., Senior, C. A., Bellucci, A., Bao, Q., Chang, P.,
868   Corti, S., Fučkar, N. S., Guemas, V., von Hardenberg, J., Hazeleger, W., Kodama, C.,
869   Koenigk, T., Leung, L. R., Lu, J., Luo, J.-J., Mao, J., Mizielinski, M. S., Mizuta, R., Nobre,

870   P., Satoh, M., Scoccimarro, E., Semmler, T., Small, J., and von Storch, J.-S.: High
871   Resolution Model Intercomparison Project (HighResMIP v1.0) for CMIP6, Geosci. Model
872   Dev., 9, 4185–4208, https://doi.org/10.5194/gmd-9-4185-2016, 2016.

873 Haarsma, R., Acosta, M., Bakhshi, R., Bretonnière, P.-A., Caron, L.-P., Castrillo, M., Corti,
874   S., Davini, P., Exarchou, E., Fabiano, F., Fladrich, U., Fuentes Franco, R., García-Serrano,
875   J., von Hardenberg, J., Koenigk, T., Levine, X., Meccia, V. L., van Noije, T., van den Oord,
876   G., Palmeiro, F. M., Rodrigo, M., Ruprich-Robert, Y., Le Sager, P., Tourigny, E., Wang, S.,
877   van Weele, M., and Wyser, K.: HighResMIP versions of EC-Earth: EC-Earth3P and
878   EC-Earth3P-HR – description, model computational performance and basic validation,
879   Geosci. Model Dev., 13, 3507–3527, https://doi.org/10.5194/gmd-13-3507-2020, 2020.

880 Hawcroft, M., Haywood, J.M., Collins, M., Jones, A., Jones, A.C. and Stephens, G., 2017.
881   Southern Ocean albedo, inter-hemispheric energy transports and the double ITCZ: Global
882   impacts of biases in a coupled model. Climate Dynamics, 48, 2279–2295,
883   https://doi.org/10.1007/s00382-016-3205-5, 2017.

884 Hazeleger, W., Wang, X., Severijns, C., Ştefănescu, S., Bintanja, R., Sterl, A., Wyser, K.,
885   Semmler, T., Yang, S., van den Hurk, B., van Noije, T., van der Linden, E., and van der
886   Wiel, K.: EC-Earth V2.2: description and validation of a new seamless earth system
887   prediction model, Clim. Dynam., 39, 2611–2629, 2012.

888 Hewitt, H. T., Bell, M. J., Chassignet, E. P., Czaja, A., Ferreira, D., Griffies, S. M., Hyder, P.,
889   McClean, J. L., New, A. L., and Roberts, M. J.: Will high-resolution global ocean models
890   benefit coupled predictions on short-range to climate timescales?, Ocean Model., 120,
891   120–136, https://doi.org/10.1016/j.ocemod.2017.11.002, 2017.

892 Hersbach, H., Bell, B., Berrisford, P., Biavati, G., Horányi, A., Muñoz Sabater, J., Nicolas, J.,
893   Peubey, C., Radu, R., Rozum, I., Schepers, D., Simmons, A., Soci, C., Dee, D., and
894   Thépaut, J.-N.: ERA5 monthly averaged data on pressure levels from 1979 to present,
895   Copernicus Climate Change Service (C3S) Climate Data Store (CDS) [data set],
896   https://doi.org/10.24381/cds.6860a573, 2019.

897 Hersbach, H., Bell, B., Berrisford, P., Hirahara, S., Horányi, A., Muñoz-Sabater, J., Nicolas,
898   J., Peubey, C., Radu, R., Schepers, D., Simmons, A., Soci, C., Abdalla, S., Abellan, X.,
899   Balsamo, G., Bechtold, P., Biavati, G., Bidlot, J., Bonavita, M., Chiara, G. D., Dahlgren, P.,
900   Dee, D., Diamantakis, M., Dragani, R., Flemming, J., Forbes, R., Fuentes, M., Geer, A.,

Haimberger, L., Healy, S., Hogan, R. J., Hólm, E., Janisková, M., Keeley, S., Laloyaux, P., Lopez, P., Lupu, C., Radnoti, G., de Rosnay, P., Rozum, I., Vamborg, F., Villaume, S., and Thépaut, J.: The ERA5 global reanalysis, Q. J. Roy. Meteor. Soc., 146, 1999–2049, https://doi.org/10.1002/qj.3803, 2020 (data available at: https://www.ecmwf.int/en/forecasts/dataset/ecmwf-reanalysis-v5, last access: 23 January 2020).

Hodges, K. I., Lee, R. W., and Bengtsson, L.: A comparison of extratropical cyclones in recent reanalyses ERA-Interim, NASA MERRA, NCEP CFSR, and JRA-25, J. Climate, 24, 4888–4906, https://doi.org/10.1175/2011JCLI4097.1, 2011.

Hohenegger, C., Korn, P., Linardakis, L., Redler, R., Schnur, R., Adamidis, P., Bao, J., Bastin, S., Behravesh, M., Bergemann, M. and Biercamp, J.: ICON-Sapphire: simulating the components of the Earth system and their interactions at kilometer and subkilometer scales. Geoscientific Model Development Discussions, 1–42, https://doi.org/10.5194/gmd-16-779-2023, 2022.

Hourdin, F., Williamson, D., Rio, C., Couvreux, F., Roehrig, R., Villefranque, N., Musat, I., Fairhead, L., Diallo, F. B. and Volodina, V.: Process-based climate model development harnessing machine learning: II. Model calibration from single column to global. Journal of Advances in Modeling Earth Systems, 13(6), e2020MS002225, https://doi.org/10.1029/2020MS002225, 2021.

Hwang, Y. T. and Frierson, D. M.: Link between the double-Intertropical Convergence Zone problem and cloud biases over the Southern Ocean, P. Natl. Acad. Sci. USA, 110, 4935–4940, https://doi.org/10.1073/pnas.1213302110, 2013.

Hyder, P., Edwards, J. M., Allan, R. P., Hewitt, H. T., Bracegirdle, T. J., Gregory, J. M., Wood, R. A., Meijers, A. J., Mulcahy, J., Field, P., and Furtado, K.: Critical Southern Ocean climate model biases traced to atmospheric model cloud errors, Nat. Commun., 9, 1–17, https://doi.org/10.1038/s41467-018-05634-2, 2018.

Jacob, D., Petersen, J., Eggert, B., Alias, A., Christensen, O. B., Bouwer, L. M., Braun, A., Colette, A., Déqué, M., Georgievski, G. and Georgopoulou, E.: EURO-CORDEX: new high-resolution climate change projections for European impact research. Regional Environmental Change, 14, 563–578, https://doi.org/10.1007/s10113-013-0499-2, 2014.

931 Kirtman, B. P., Bitz, C., Bryan, F., Collins, W., Dennis, J., Hearn, N., Kinter, J. L., Loft, R.,
932   Rousset, C., Siqueira, L., and Stan, C.: Impact of ocean model resolution on CCSM climate
933   simulations, Clim. Dynam., 39, 1303–1328, https://doi.org/10.1007/s00382-012-1500-3,
934   2012.

935 Kriegler, E., Bauer, N., Popp, A., Humpenöder, F., Leimbach, M., Strefler, J., Baumstark, L.,
936   Bodirsky, B.L., Hilaire, J., Klein, D., and Mouratiadou, I.: Fossil-fueled development
937   (SSP5): An energy and resource intensive scenario for the 21st century. Global
938   Environmental Change, 42, 297–315, https://doi.org/10.1016/j.gloenvcha.2016.05.015,
939   2017.

940 Lee, R.W., Woollings, T. J., Hoskins, B. J., Williams, K. D., O'Reilly, C. H. and Masato, G.:
941   Impact of Gulf Stream SST biases on the global atmospheric circulation. Climate Dynamics,
942   51, 3369–3387, https://doi.org/10.1007/s00382-018-4083-9, 2018.

943 Lofverstrom, M., Fyke, J. G., Thayer-Calder, K., Muntjewerf, L., Vizcaino, M., Sacks, W. J.,
944   Lipscomb, W. H., Otto-Bliesner, B. L. and Bradley, S. L.: An efficient ice sheet/Earth
945   system model spin-up procedure for CESM2-CISM2: Description, evaluation, and broader
946   applicability. Journal of Advances in Modeling Earth Systems, 12(8), e2019MS001984,
947   https://doi.org/10.1029/2019MS001984, 2020.

948 Lyu, G., Köhl, A., Matei, I. and Stammer, D.: Adjoint-based climate model tuning:
949   Application to the planet simulator. Journal of Advances in Modeling Earth Systems, 10(1),
950   207–222, https://doi.org/10.1002/2017MS001194, 2018.

951 Ma, X., Chang, P., Saravanan, R., Montuoro, R., Nakamura, H., Wu, D., Lin, X. and Wu, L.:
952   Importance of resolving Kuroshio front and eddy influence in simulating the North Pacific
953   storm   track.   Journal   of   Climate,   30(5),   1861–1880,
954   https://doi.org/10.1175/JCLI-D-16-0154.1, 2017.

955 Madec, G.: NEMO reference manual, ocean dynamic component: NEMO-OPA, Note du Pôle
956   modélisation, Inst. Pierre Simon Laplace, France, 2008.

957 Madec, G. and the NEMO team: NEMO ocean engine version 3.6 stable, Note du Pôle de
958   modélisation de l'Institut Pierre-Simon Laplace No. 27, ISSN: 1288–1619, 2016.

959 Manubens-Gil, D., Vegas-Regidor, J., Prodhomme, C., Mula-Valls, O. and Doblas-Reyes, F.
960   J.: Seamless management of ensemble climate prediction experiments on HPC platforms. In

961   2016 International Conference on High Performance Computing & Simulation (HPCS),

962   895–900, 2016, https://doi.org/10.1109/HPCSim.2016.7568429, 2016.

963   Mauritsen, T., Stevens, B., Roeckner, E., Crueger, T., Esch, M., Giorgetta, M., Haak, H.,

964   Jungclaus, J., Klocke, D., Matei, D. and Mikolajewicz, U.: Tuning the climate of a global

965   model.   Journal   of   advances   in   modeling   Earth   systems,   4(3),

966   https://doi.org/10.1029/2012MS000154, 2012.

967   McDougall, T. J., Barker, P. M., Holmes, R. M., Pawlowicz, R., Griffies, S. M. and Durack, P.

968   J.: The interpretation of temperature and salinity variables in numerical ocean model output

969   and the calculation of heat fluxes and heat content. Geoscientific Model Development,

970   14(10), 6445–6466, https://doi.org/10.5194/gmd-14-6445-2021, 2021.

971   McGee, D., Moreno-Chamarro, E., Marshall, J. and Galbraith, E.D.: Western US lake

972   expansions during Heinrich stadials linked to Pacific Hadley circulation. Science advances,

973   4(11), p.eaav0118, https://doi.org/10.1126/sciadv.aav0118, 2018.

974   Meehl, G.A., Yang, D., Arblaster, J.M., Bates, S.C., Rosenbloom, N., Neale, R., Bacmeister,

975   J., Lauritzen, P.H., Bryan, F., Small, J. and Truesdale, J.: Effects of model resolution,

976   physics, and coupling on Southern Hemisphere storm tracks in CESM1. 3. Geophysical

977   Research Letters, 46(21), 12408–12416, https://doi.org/10.1029/2019GL084057, 2019.

978   Merlis, T. M. and Khatiwala, S.: Fast dynamical spin-up of ocean general circulation models

979   using   Newton–Krylov   methods.   Ocean   Modelling,   21(3-4),   97–105,

980   https://doi.org/10.1016/j.ocemod.2007.12.001, 2008.

981   Milinski, S., Bader, J., Haak, H., Siongco, A. C., and Jungclaus, J. H.: High atmospheric

982   horizontal resolution eliminates the wind-driven coastal warm bias in the southeastern

983   tropical   Atlantic: Geophys.   Res.   Lett.,   43,   10455–10462,

984   https://doi.org/10.1002/2016GL070530, 2016.

985   Moreno-Chamarro, E.: Data for "The very-high resolution configuration of the EC-Earth

986   global model for HighResMIP", Zenodo [data set, last access: 10 July 2024],

987   https://doi.org/10.5281/zenodo.12078052, 2024.

988   Moreno-Chamarro, E., Caron, L. P., Ortega, P., Tomas, S. L. and Roberts, M. J.: Can we trust

989   CMIP5/6 future projections of European winter precipitation?: Environmental Research

990   Letters, 16(5), 054063, https://doi.org/10.1088/1748-9326/abf28a, 2021.

Moreno-Chamarro, E., Caron, L. P., Loosveldt Tomas, S., Vegas-Regidor, J., Gutjahr, O., Moine, M. P., Putrasahan, D., Roberts, C. D., Roberts, M. J., Senan, R. and Terray, L.: Impact of increased resolution on long-standing biases in HighResMIP-PRIMAVERA climate models: Geoscientific Model Development, 15(1), 269–289, https://doi.org/10.5194/gmd-15-269-2022, 2022.

Moreton, S., Ferreira, D., Roberts, M. and Hewitt, H.: Air-Sea Turbulent Heat Flux Feedback Over Mesoscale Eddies. Geophysical Research Letters, 48(20), e2021GL095407, 2021.

Pawlowicz, R.: Key physical variables in the ocean: temperature, salinity, and density. Nature Education Knowledge, 4(4), 13, https://doi.org/10.1029/2021GL095407, 2013.

Pershing, A.J., Alexander, M.A., Hernandez, C.M., Kerr, L.A., Le Bris, A., Mills, K.E., Nye, J.A., Record, N.R., Scannell, H.A., Scott, J.D. and Sherwood, G.D.: Slow adaptation in the face of rapid warming leads to collapse of the Gulf of Maine cod fishery. Science, 350(6262), 809–812, https://doi.org/10.1126/science.aac9819, 2015.

Rai, S., Hecht, M.W., Maltrud, M.E. and Aluie, H.: Scale-dependent Air-Sea Mechanical Coupling: Resolution Mismatch and Spurious Eddy-Killing, https://doi.org/10.22541/essoar.167525271.13326232/v1, 2023.

Rackow, T., Pedruzo-Bagazgoitia, X., Becker, T., Milinski, S., Sandu, I., Aguridan, R., Bechtold, P., Beyer, S., Bidlot, J., Boussetta, S., Diamantakis, M., Dueben, P., Dutra, E., Forbes, R., Goessling, H. F., Hadade, I., Hegewald, J., Keeley, S., Kluft, L., Koldunov, N., Koldunov, A., Kölling, T., Kousal, J., Mogensen, K., Quintino, T., Polichtchouk, I., Sármány, D., Sidorenko, D., Streffing, J., Sützl, B., Takasuka, D., Tietsche, S., Valentini, M., Vannière, B., Wedi, N., Zampieri, L., and Ziemen, F.: Multi-year simulations at kilometre scale with the Integrated Forecasting System coupled to FESOM2.5/NEMOv3.4, EGUsphere [preprint], https://doi.org/10.5194/egusphere-2024-913, 2024.

Renault, L., Lemarié, F. and Arsouze, T.: On the implementation and consequences of the oceanic currents feedback in ocean–atmosphere coupled models. Ocean Modelling, 141, 101423, https://doi.org/10.1016/j.ocemod.2019.101423, 2019.

Renault, L., Marchesiello, P., & Contreras, M.: Coaction of top and bottom drags in Gulf Stream dynamics. Journal of Geophysical Research: Oceans, 128, e2022JC018939. https://doi. org/10.1029/2022JC018939, 2023.

1021   Richter, I.: Climate model biases in the eastern tropical oceans: Causes, impacts and ways

1022   forward, Wires Clim. Change, 6, 345–358, https://doi.org/10.1002/wcc.338, 2015.

1023   Roberts, C. D., Senan, R., Molteni, F., Boussetta, S., Mayer, M., and Keeley, S. P. E.: Climate

1024   model configurations of the ECMWF Integrated Forecasting System (ECMWF-IFS cycle

1025   43r1) for HighResMIP, Geosci. Model Dev., 11, 3681–3712,

1026   https://doi.org/10.5194/gmd-11-3681-2018, 2018.

1027   Roberts, M. J., Baker, A., Blockley, E. W., Calvert, D., Coward, A., Hewitt, H. T., Jackson, L.

1028   C., Kuhlbrodt, T., Mathiot, P., Roberts, C. D. and Schiemann, R.: Description of the

1029   resolution hierarchy of the global coupled HadGEM3-GC3. 1 model as used in CMIP6

1030   HighResMIP experiments. Geoscientific Model Development, 12(12), 4999–5028,

1031   https://doi.org/10.5194/gmd-12-4999-2019, 2019.

1032   Roberts, M. J., Camp, J., Seddon, J., Vidale, P. L., Hodges, K., Vanniere, B., Mecking, J.,

1033   Haarsma, R., Bellucci, A., Scoccimarro, E., and Caron, L. P.: Impact of model resolution on

1034   tropical cyclone simulation using the HighResMIP–PRIMAVERA multimodel ensemble, J.

1035   Climate, 33, 2557–2583, https://doi.org/10.1175/JCLI-D-19-0639.1, 2020a.

1036   Roberts, M. J., Jackson, L. C., Roberts, C. D., Meccia, V., Docquier, D., Koenigk, T., Ortega,

1037   P., Moreno-Chamarro, E., Bellucci, A., Coward, A., and Drijfhout, S.: Sensitivity of the

1038   Atlantic meridional overturning circulation to model resolution in CMIP6 HighResMIP

1039   simulations and implications for future changes, J. Adv. Model. Earth Sy., 12,

1040   e2019MS002014, https://doi.org/10.1029/2019MS002014, 2020b.

1041   Roberts, M. J., Vidale, P. L., Senior, C., Hewitt, H. T., Bates, C., Berthou, S., Chang, P.,

1042   Christensen, H. M., Danilov, S., Demory, M. E., and Griffies, S. M.: The benefits of global

1043   high resolution for climate simulation: process understanding and the enabling of

1044   stakeholder decisions at the regional scale, B. Am. Meteorol. Soc., 99, 2341–2359,

1045   https://doi.org/10.1175/BAMS-D-15-00320.1, 2018.

1046   Saba, V.S., Griffies, S.M., Anderson, W.G., Winton, M., Alexander, M.A., Delworth, T.L.,

1047   Hare, J.A., Harrison, M.J., Rosati, A., Vecchi, G.A. and Zhang, R.: Enhanced warming of

1048   the Northwest Atlantic Ocean under climate change. Journal of Geophysical Research:

1049   Oceans, 121(1), 118–132, https://doi.org/10.1002/2015JC011346, 2016.

1050   Segura, H., Hohenegger, C., Wengel, C. and Stevens, B.: Learning by doing: Seasonal and

1051   diurnal features of tropical precipitation in a global-coupled storm-resolving model.

Geophysical Research Letters, 49(24), p.e2022GL101796, https://doi.org/10.1029/2022GL101796, 2022.

Small, R. J., Bryan, F. O., Bishop, S. P. and Tomas, R. A.: Air–sea turbulent heat fluxes in climate models and observational analyses: What drives their variability?. Journal of Climate, 32(8), 2397–2421, https://doi.org/10.1175/JCLI-D-18-0576.1, 2019.

Stengel, M., Stapelberg, S., Sus, O., Finkensieper, S., Würzler, B., Philipp, D., Hollmann, R., Poulsen, C., Christensen, M., and McGarragh, G.: Cloud_cci Advanced Very High Resolution Radiometer post meridiem (AVHRR-PM) dataset version 3: 35 year climatology of global cloud and radiation properties, Earth Syst. Sci. Data, 12, 41–60, https://doi.org/10.5194/essd-12-41-2020, 2020 (data available at: https://climate.esa.int/en/projects/cloud/data/, last access: 10 March 2021).

Sun, X. and Wu, R.: Spatial scale dependence of the relationship between turbulent surface heat flux and SST. Climate Dynamics, 58(3), 1127–1145, https://doi.org/10.1007/s00382-021-05957-9, 2022.

Tian, B. and Dong, X.: The double-ITCZ bias in CMIP3, CMIP5, and CMIP6 models based on annual mean precipitation, Geophys. Res. Lett., 47, e2020GL087232, https://doi.org/10.1029/2020GL087232, 2020.

Tintó Prims, O., M. C. Acosta, A. M. Moore, M. Castrillo, K. Serradell, A. Cortés and F. J. Doblas-Reyes: How to use mixed precision in ocean models: exploring a potential reduction of numerical precision in NEMO 4.0 and ROMS 3.6. Geoscientific Model Development, 12, 3135-3148, https://doi.org/10.5194/gmd-12-3135-2019, 2019a.

Tintó Prims O., M. Castrillo, M. C. Acosta, O. Mula-Valls, A. Sanchez Lorente, K. Serradell, A. Cortés and F. J. Doblas-Reyes: Finding, analysing and solving MPI communication bottlenecks in Earth System models. Journal of Computational Sciences, 36, 100864, https://doi.org/10.1016/j.jocs.2018.04.015, 2019b.

Todd, R. E. and Ren, A. S.: Warming and lateral shift of the Gulf Stream from in situ observations since 2001. Nature Climate Change, 13(12), 1348–1352, https://doi.org/10.1038/s41558-023-01835-w, 2023.

Tomita, H., Hihara, T., Kako, S.I., Kubota, M. and Kutsuwada, K.: An introduction to J-OFURO3, a third-generation Japanese ocean flux data set using remote-sensing observations. Journal of Oceanography, 75(2), 171–194,

https://doi.org/10.1007/s10872-018-0493-x, 2019 (data available at: https://www.j-ofuro.com/en/dataset/, last access: 14 March 2024).

Tsartsali, E. E., Haarsma, R. J., Athanasiadis, P. J., Bellucci, A., de Vries, H., Drijfhout, S., de Vries, I. E., Putrahasan, D., Roberts, M. J., Sanchez–Gomez, E. and Roberts, C. D.: Impact of resolution on the atmosphere–ocean coupling along the Gulf Stream in global high resolution models. Climate Dynamics, 58(11–12), 3317–3333, https://doi.org/10.1007/s00382-021-06098-9, 2022.

Valcke, S. and Morel, T.: OASIS and PALM, the CERFACS couplers, Tech. rep., CERFACS, 2006.

Vancoppenolle, M., Bouillon, S., Fichefet, T., Goosse, H., Lecomte, O., Morales Maqueda, M. A., and Madec, G.: The Louvain-la-Neuve sea ice model, Notes du pole de modélisation, Institut Pierre-Simon Laplace (IPSL), Paris, France, No. 31, 2012.

Varma, V., Morgenstern, O., Field, P., Furtado, K., Williams, J., and Hyder, P.: Improving the Southern Ocean cloud albedo biases in a general circulation model, Atmos. Chem. Phys., 20, 7741–7751, https://doi.org/10.5194/acp-20-7741-2020, 2020.

Vidale, P. L., Hodges, K., Vannière, B., Davini, P., Roberts, M. J., Strommen, K., Weisheimer, A., Plesca, E., and Corti, S.: Impact of stochastic physics and model resolution on the simulation of Tropical Cyclones in climate GCMs, J. Climate, 34, 4315–4341, https://doi.org/10.1175/JCLI-D-20-0507.1, 2021.

Wan, H., Rasch, P. J., Zhang, K., Qian, Y., Yan, H. and Zhao, C.: Short ensembles: An efficient method for discerning climate-relevant sensitivities in atmospheric general circulation models. Geoscientific Model Development, 7(5), 1961–1977, https://doi.org/10.5194/gmd-7-1961-2014, 2014.

Wengel, C., Lee, S. S., Stuecker, M. F., Timmermann, A., Chu, J. E., and Schloesser, F.: Future high-resolution El Niño/Southern Oscillation dynamics, Nat. Clim. Change, 1–8, https://doi.org/10.1038/s41558-021-01132-4, 2021.

Williamson, D., Goldstein, M., Allison, L., Blaker, A., Challenor, P., Jackson, L. and Yamazaki, K.: History matching for exploring and reducing climate model parameter space using observations and a large perturbed physics ensemble. Climate Dynamics, 41, 1703–1729, https://doi.org/10.1007/s00382-013-1896-4, 2013.

Woollings, T., Hoskins, B., Blackburn, M., Hassell, D. and Hodges, K.: Storm track sensitivity to sea surface temperature resolution in a regional atmosphere model. Climate Dynamics, 35, 341–353, https://doi.org/10.1007/s00382-009-0554-3, 2010.

Xepes-Arbós, X., G. van den Oord, M. C. Acosta and G. D. Carver: Evaluation and optimisation of the I/O scalability for the next generation of Earth system models: IFS CY43R3 and XIOS 2.0 integration as a case study. Geoscientific Model Development, 15, 379–394, https://doi.org/10.5194/gmd-15-379-2022, 2022.

Zhang, J. and Rothrock, D. A.: Modeling global sea ice with a thickness and enthalpy distribution model in generalized curvilinear coordinates, Mon. Weather Rev., 131, 845–861, https://doi.org/10.1175/1520-0493(2003)131<0845:Mgsiwa>2.0.Co;2, 2003 (data available at: https://psc.apl.washington.edu/zhang/Global_seaice/model.html, last access: 6 March 2019).

Zhang, W., Villarini, G., Scoccimarro, E., Roberts, M., Vidale, P. L., Vanniere, B., Caron, L. P., Putrasahan, D., Roberts, C., Senan, R., and Moine, M. P.: Tropical cyclone precipitation in the HighResMIP atmosphere-only experiments of the PRIMAVERA Project, Clim. Dynam., 57, 253–273, https://doi.org/10.1007/s00382-021-05707-x, 2021.